**Multimodal interrogation of ventral pallidum projections reveals projection-specific signatures and opposite roles in cocaine withdrawal**

Nimrod Bernat, MSc[1,2]*, Rianne Campbell, PhD[3]*, Hyungwoo Nam, PhD[3], Mahashweta Basu, PhD[4,5], Tal Odesser, BSc[1], Gal Elyasaf, BSc[1], Michel Engeln, PhD[3,6], Ramesh Chandra, PhD[3], Shana Golden, BSc[1], Seth Ament, PhD[4,5], Mary Kay Lobo, PhD[3#], Yonatan M. Kupchik, PhD[1,2#]

[1]Department of Medical Neurobiology, Faculty of Medicine, The Institute for Medical Research Israel-Canada (IMRIC), The Hebrew University of Jerusalem, Israel

[2]IMRIC Center for Addiction Research (ICARe), The Hebrew University of Jerusalem

[3]Department of Anatomy and Neurobiology, University of Maryland School of Medicine, Baltimore, MD, USA

[4]Department of Psychiatry, University of Maryland School of Medicine, Baltimore, MD, USA.

[5]Institute for Genome Sciences, University of Maryland School of Medicine, Baltimore, MD, USA.

[6]University of Bordeaux, CNRS, IMN, UMR 5293, F-33000 Bordeaux, France.

*Equal contribution

[#]To whom correspondence should be addressed

Running title – Opposite roles of VP projections

Contact details of YMK – Department of Medical Neurobiology, Room 6-48, Faculty of Medicine, Ein Karem Campus, The Hebrew University of Jerusalem, Israel, 9112102. Email – Yonatan.kupchik@mail.huji.ac.il. Phone - +972-2-6757551

Abstract – 161 words

Introduction – 330 words

Methods – 2027 words

Results – 2541 words

Discussion – 1129 words

Legends – 1657 words

## Abstract

The ventral pallidum (VP) is central to reward seeking and withdrawal from drugs of abuse. A characteristic of the VP is the diversity of its projection targets. Yet, it remains unknown whether different VP projections also differ in other aspects, such as their transcriptome, physiology and relevance to drug reward. In this study we perform a multimodal dissection of four major projections of the VP – to the lateral hypothalamus ($VP_{\rightarrow LH}$), ventral tegmental area ($VP_{\rightarrow VTA}$), lateral habenula ($VP_{\rightarrow LHb}$) and mediodorsal thalamus ($VP_{\rightarrow MDT}$) – with physiological, anatomical, genetic and behavioral tools and show significant differences between projections in all aspects. Specifically, the $VP_{\rightarrow LH}$ and $VP_{\rightarrow VTA}$ projections show minimal overlap and stand out as having opposite properties – $VP_{\rightarrow LH}$ neurons show higher excitability compared to $VP_{\rightarrow VTA}$ neurons, different pattern of inputs and differentially expressed genes. Moreover, inhibition of $VP_{\rightarrow LH}$ projections diminishes, while inhibition of $VP_{\rightarrow VTA}$ enhances cocaine preference after cocaine withdrawal. This demonstrates that VP projections are heterogenous neuron populations with different roles in cocaine withdrawal.

## Introduction

The ventral pallidum (VP) is a central hub in the basal ganglia and plays important roles in motivation, reward, and addiction[1–3]. It consists mainly of GABAergic neurons, with a minority of glutamatergic and cholinergic neurons[1]. Its neurons are also sometimes categorized by a neuropeptide they release[4] or the expression of a particular receptor[5] or protein[1,2,6,7].

In addition to the intricate cellular composition, the VP also shows complex connectivity. It receives mainly inhibitory inputs from various limbic regions[1] while having a wide range of downstream targets, including dense projections to the ventral tegmental area ($VP_{\rightarrow VTA}$), the lateral hypothalamus ($VP_{\rightarrow LH}$), the mediodorsal thalamus ($VP_{\rightarrow MDT}$) and the lateral habenula ($VP_{\rightarrow LHb}$)[1]. Previous work has shown that VP projection neurons exert different roles in rewarding and aversive behaviors[1,8–12]. Despite these distinct roles in behavior, it is theorized that different VP projections are composed largely of the same neuronal composition, possibly even with significant overlap between the projection subpopulations.

The development of new technologies such as rabies-based tracing[13,14], single-cell RNA sequencing[15] and cell-specific optogenetics[16–18] or chemogenetics[19] reveals in recent studies an increasing heterogeneity of neurons residing within the same brain region, defined by their connectivity patterns, gene expression, physiology, morphology and more[20,21]. The high complexity of these methods has driven most studies to focus on one modality when analyzing the heterogeneity of neurons in a certain region. In particular, heterogeneity is often described either based on intracellular properties (gene expression, physiology, etc.) or on system-level connectivity, without integrating these two levels of complexity. As neurons are multimodal entities there is a need for a multimodal interrogation of neuronal heterogeneity.

In this collaborative work we integrate multilevel approaches to examine whether the different projections of the VP to the VTA, LH, MDT and LHb are separate neuronal subpopulations based on their inputs, physiology, transcriptome and behavioral relevance. Our data highlight the $VP_{\rightarrow VTA}$ and $VP_{\rightarrow LH}$ projections as highly distinct in these parameters, suggesting these two projections of the VP may be different types of neurons.

## Methods

Experimental subjects – For electrophysiology, neural tracing and behavioral experiments, subjects were naïve C57bl6/J wildtype male and female mice who were approximately 8 weeks old at the beginning of the experiments. A 12-hour reversed light/dark cycle was maintained, with the lights turned off at 8:00 am. Experimental procedures were conducted during dark hours. Mice were group-housed and nesting/enrichment material was available. Experimentation began after a minimum of 7 days of acclimation to animal facility. All experimental procedures were approved by the Authority for Biological and Biomedical Models in the Hebrew university. For projection-specific gene expression analysis, adult (7-8 weeks old) male RiboTag (RT)+/+ mice (Rpl22tm1.1Psam/J) on a C57Bl/6 background were used. RiboTag mice were given food and water ad libitum throughout the study. These studies were conducted in accordance with guidelines of the Institutional Animal Care and Use Committees at University of Maryland School of Medicine.

Stereotaxic microinjections - Mice were anesthetized with isoflurane and fixed in a stereotaxic frame (Kopf, Model 940). Viruses or red Retrobeads™ (Lumafluor, Durham,

North Carolina) were microinjected into one or more of the following structures - the MDT (coordinates in millimeters relative to Bregma: anterior/posterior -1.5, medial/lateral ±0.47, dorsal/ventral -3.63), LHb (A/P -1.8, M/L ±0.7, D/V -2.91), LH (A/P -0.3, M/L ±0.9, D/V -5.5), VTA (A/P -2.9, M/L ±0.5, D/V -4.53), VP (A/P 0.7, M/L ±1.2, D/V -5.21) and NAc (A/P 1.8, M/L ±1.0, D/V -4.6) (see below for details on the injections in each experiment). Injections were performed bilaterally by drilling bilateral holes into the skull and then microinjecting the viral constructs [through a 33 ga NanoFil syringe (World Precision Instruments; 300 nl per hemisphere, 100 nl/min, needle retracted 5 min after injection terminated)] or Retrobeads [through a 30 ga syringe (Hamilton: 300 nl per hemisphere, 300 nl/min, needle retracted 5 min after injection terminated)] into the target structure.

Circuit-specific gene expression analysis was performed using retrograde AAV-Cre virus in combination with Ribotag mice. Briefly, anesthetized RiboTag RT +/+ mice were bilaterally injected with AAV5-Cre viruses (AAV sterotype 5 AAV5.hSyn.HI.eGFP-Cre.WPRE.SV40 (Addgene; #105540) at the following coordinates: VP (from Bregma; 10° angle, anterior/posterior: AP +0.9, medial/lateral: ML ±2.2, dorsal/ventral: DV -5.3), MDT (from Bregma; 10° angle, AP: -0.8, ML: ±1.2, DV: -3.7), VTA (from Bregma; 7° angle, AP: - 3.2, ML: ±1, DV: -4.6), LHb (from Bregma; 10° angle, AP: -1.2, ML: ±0.7, DV: - 3.1) and LH (from Bregma; 10° angle, AP: -0.7, ML: ±1.4, DV: - 5.2).

Double-labeling experiments – Each mouse was injected with two different retrograde tracers, rAAV-GFP and rAAV-RFP (ELSC viral core, The Hebrew University, Israel). Each virus was injected bilaterally (300 nl per hemisphere) into one of the VP targets tested here. Two weeks after microinjections mice were anesthetized with Pental (CTS Chemical Industries, Israel) and perfused with 4% paraformaldehyde (PFA). Sections of the VP (40 μm) were prepared using a sliding microtome (Leica, model SM2010R) and mounted on slides. The sections were scanned with Nikon ECLIPSE-NiE fluorescent microscope and scans were analyzed using ImageJ (NIH).

Whole-brain mapping of inputs to VP projections – To label monosynaptic inputs to specific VP projections we used the "The Relationship between Inputs and Outputs" (TRIO) technique[13]. Mice were first injected with a retrograde virus expressing Cre recombinase (rAAV-Cre; ELSC viral core, The Hebrew University, Israel) into one of the four targets of the VP examined here (300 nl). We also injected these mice with a cocktail of two helper viruses expressing the TVA receptor (AAV-FLEx-TVA-mCherry) and the rabies glycoprotein (AAV-FLEx-RG) (total of 500 nl, 250 nl per virus) into the VP.

Two weeks after these injections we injected mice with the modified rabies virus (500 nl) into the VP. We allowed the virus 7 days to spread before anesthetizing and perfusing the mice with PFA as described above. Brains were then post-fixed with 4% PFA overnight at 4 °C. Tissue clearing and staining were performed according to the detailed protocol available at http://idisco.info. Briefly, brains were dehydrated, bleached to reduce background autofluorescence, rehydrated, then incubated with rabbit anti-RFP antibody (1:1000, Rockland, Cat# 600-401-379) and chicken anti-GFP antibody (1:2000, Aves labs, Ca# GFP1010) for 5 days, followed by washing and incubation in Cy3 conjugated anti rabbit secondary antibody (1:500, Jackson ImmunoResearch, Cat# 711-165-152) and Cy5 conjugated anti chicken secondary antibody (1:400, Jackson ImmunoResearch, Cat# 703-175-155) for 5 days. Following additional washing, brains were dehydrated and cleared in methanol and dichloromethane, then refractive index matching occurred in dibenzyl ether. Brains were imaged at x4 magnification, 0.35 numerical aperture, in the vertical orientation on a LaVision Ultramicroscope II light-sheet microscope with a near-isotropic xyz resolution of 1.6 μm × 1.6 μm × 2 μm. Images were acquired with a 488 nm laser for an autofluorescence reference channel, and 561 nm and 642 nm lasers for acquisition of secondary antibody fluorescence. The ClearMap Python package (www.github.com/christophkirst/clearmap) was used for cell detection and registration of cell coordinates onto the Allen Brain Atlas. Data analysis occurred on an Antec P110 Silent Workstation running Ubuntu 20.04LTS, and followed steps outlined in ClearMap documentation. Briefly, data were downsampled and the Elastix toolbox (http://elastix.isi.uu.nl/) was used to perform automated 3D affine and B-spline transformation to register the autofluorescence signal channel to the 25 μm resolution Allen Brain Atlas reference, and to correct for any motion between imaging of the autofluorescence and signal channel images. Elastix's 'pixel classification' machine learning workflow was used to teach a model to segment input neurons from background, which later was used in Headless mode in ClearMap to detect input neurons. The Transformix module of the Elastix toolbox was then used to apply transformation vectors from the registration step to cellular coordinates, and cell counts for each region were calculated.

RNA-Sequencing and Bioinformatics- Three weeks following viral injections, VP tissue was collected from Ribotag mice infused with Retrograde-Cre virus (AAV5-Cre). Projection-specific RNA isolation was performed using polyribosome

immunoprecipitation as described previously[22,23]. Briefly, pooled tissue from RiboTag (RT)+/+ mice with virally mediated Cre expression in VP projection neurons (n= 5 mice per sample) or in VP was homogenized and 800 µL of the supernatant was incubated in HA-coupled magnetic beads (Invitrogen: 100.03D; Covance: MMS-101R) overnight at 4°C. Magnetic beads were washed using high salt buffer. Following TRK lysis buffer, RNA was extracted with the RNeasy Micro kit (Qiagen: 74004). Libraries were prepared from 10 ng of RNA using the NEBNext Ultra kit (New England BioLabs, Ipswich, MA, USA) and sequenced on an Illumina HiSeq 4000 with a 75 bp paired-end read. RNA-sequencing data are available through the Gene Expression Omnibus database (GEO accession number: GSE218580).

A total of 75–110 million reads were obtained for each sample. Reads were aligned to the mouse genome using TopHat and the number of reads that aligned to the predicted coding regions was determined using HTSeq. Significant differential expression was assessed using Limma by comparing VP projection neuron samples to total VP. Genes with the absolute value of log fold change (LFC) ≥ 0.3 and an uncorrected p-value<0.05 in the pairwise comparisons were used for downstream analysis (**Supplementary Table 1**). Cytoscape 3.7.2 software was used for downstream analysis: transcriptional regulator networks were identified using the iRegulon app and Gene Ontology functional enrichment analysis was performed using the BiNGO app (**Supplementary Table 2**). From these lists, top GO terms were selected based off of highest $-\log_{10}$(adjusted-p-value), and top upstream regulators were selected based on the number of predicted targets DEGs.

Slice preparation - As described before [24–26]. Mice were anesthetized with 150 mg/kg Ketamine-HCl and then decapitated. Coronal slices (200 µm) of the VP were prepared (VT1200S Leica vibratome) and moved to vials containing artificial cerebrospinal fluid (aCSF (in mM): 126 NaCl, 1.4 $NaH_2PO_4$, 25 $NaHCO_3$, 11 glucose, 1.2 $MgCl_2$, 2.4 $CaCl_2$, 2.5 KCl, 2.0 Na Pyruvate, 0.4 ascorbic acid, bubbled with 95% $O_2$ and 5% $CO_2$) and a mixture of 5 mM kynurenic acid and 100 mM MK-801. Slices were stored in room temperature (22-24 °C) until recording.

In vitro whole-cell recording - Recordings were performed at 32 °C (TC-344B, Warner Instrument Corporation). VP neurons were visualized using an Olympus BX51WI microscope and recorded from using glass pipettes (1.3-2.5 MΩ, World Precision Instruments) filled with internal solution (in mM: 68 KCl, 65 D-gluconic acid potassium

salt, 7.5 HEPES potassium, 1 EGTA, 1.25 MgCl2, 10 NaCl, 2.0 MgATP, and 0.4 NaGTP, pH 7.2-7.3, 275mOsm). Multiclamp 700B (Axon Instruments, Union City, CA) was used to record both membrane and action potentials and postsynaptic currents (PSCs) in whole-cell configuration. Excitability and passive membrane properties were measured in current clamp mode while synaptic activity was measured in voltage clamp mode at a holding potential of -80 mV. Recordings were acquired at 10 kHz and filtered at 2 kHz using AxoGraph X software (AxoGraph Scientific, Sydney). To evoke inhibitory PSCs (IPSCs) from NAc terminals expressing ChR2 we used a 470 nm LED light source (Mightex Systems; 0.1–1 ms in duration) directed at the slice through the x60 objective. The stimulation intensity was set to evoke 50% of maximal IPSC at −80 mV. Recordings were collected every 10 seconds. Series resistance (Rs) measured with a −2 mV hyperpolarizing step (10 ms) given with each stimulus and holding current were always monitored online. Recordings with unstable Rs or when Rs exceeded 20 MΩ were aborted.

Current clamp experiments - After penetrating the neuron, we switched to current clamp mode and recorded the resting membrane potential of the neurons and spontaneous action potentials for 60 seconds. Cells with unstable membrane potential were discarded. Action potentials were later detected by their waveform using the Axograph software, baselined and analyzed. Potentials of <20 mV in amplitude were discarded. We then applied the current step protocol - five 500 ms-long depolarization current steps ranging from 0 pA to +80 pA (20 pA intervals) were applied, inter-step interval was 3 seconds. The 5-step protocol was repeated 5 times with 3 s between repetitions. Baseline membrane potential was adjusted to be approximately -50 mV in all neurons by injecting constant current.

Cocaine conditioned place preference – Mice were first injected with rAAV-Cre in one of the 4 VP targets examined here and with an AAV encoding for the Gi-coupled DREADD, hM4Di, in a Cre-dependent manner (AAV-DIO-hM4Di-mCherry), or a sham virus (AAV2-EF1a-DIO-EYFP-WPRE-pA) into the VP. After two weeks of acclimation to the reverse light cycle and recovery from surgery, mice were trained in the unbiased cocaine conditioned place preference (CPP) paradigm as described previously [24] (**Fig. 8**). On the first day, mice were allowed to freely explore both sides of a 30 cm × 30 cm arena, divided in two, each side with a different wall pattern and floor texture. On the following days, experimental mice received one daily injection of either cocaine (15 mg/kg, i.p.) or

saline such that cocaine was always given in one side of the box (the “cocaine-paired” side) and saline in the other. Cocaine-paired sides were counterbalanced for pattern and side. Cocaine/saline injections alternated daily until each mouse received 4 of each. Control mice received 8 injections of saline. Then, mice were left in their cages for 14 days (abstinence) before being tested for their preference of the cocaine-paired side. On the test day, mice first received an injection of the DREADD ligand clozapine-N-oxide (CNO, 3 mg/kg, i.p.), were left in their home cages for 30 minutes and then put in the CPP box for 15 minutes. During the test, mice were allowed to move freely between the two sides of the arena. Movement was tracked using MediaRecorder (Noldus, the Netherlands), analyzed using Optimouse software[27] and CPP scores were calculated offline as the ratio between the difference in time spent between the cocaine-paired and unpaired sides and the total time [CPP score = (time in paired zone − time in unpaired zone)/(time in paired zone + time in unpaired zone)].

Viruses –

| Viral construct | manufacturer | Abbreviation in paper | titer | Used in figure # |
|---|---|---|---|---|
| AAV5.hSyn.HI.eGFP-Cre.WPRE.SV40 | Addgene | AAV5-Cre | 7.0E+12 | 2,3,7 |
| AAVr-hSyn-eGFP | EVCF | rAAV-GFP | 1.78E+13 | 1 |
| AAVr-hSyn-mRuby2 | EVCF | rAAV-RFP | 3.06E+13 | 1 |
| AAVr-hSyn-iCre | EVCF | rAAV-Cre | 1.10E+14 | 4,8 |
| EnvA G-Deleted Rabies-eGFP | Salk inst. | G*d*RV-GFP | 2.91E+07 | 4 |
| AAV-CA-FLEx-RG | UNC | AAV-FLEX-RG | 3.2E+12 | 4 |
| AAV-EF1a-FLEx-TVA-mCherry | UNC | AAV-FLEX-TVA | 4.3E+12 | 4 |
| AAV2-EF1a-DIO-hChR2(H134R)-EYFP | UNC | AAV-DIO-ChR | 5.7E+12 | 5 |
| AAV2-hSyn-DIO-hM4D(Gi)-mCherry | UNC | AAV-DIO-DREADDs | 3.7E+12 | 8 |
| EVCF – ELSC Vector Core Facility, The Hebrew University of Jerusalem; Salk – Salk Institute Viral Vector Core; UNC – University of North Carolina Vector Core | | | | |

Statistics and data analysis – All statistical analyses were performed using GraphPad Prism 9.2 (GraphPad Software Inc.). Parametric tests were used unless stated otherwise with p values <0.05 considered as significant. All tests are indicated in the figure legends. Data in graphs represent mean ± s.e.m.

## Results

### *Minimal overlap between VP projection neurons*

While the VP projects to the LH, VTA, MDT and LHb, it is not known whether there is any overlap between these projections, and if so to what extent. To test this we performed six experiments examining the overlap between all possible pairs of the four targets of the VP. For each pair combination we injected one retrograde virus expressing GFP (rAAV-GFP) into one of the targets and another retrograde virus expressing RFP (rAAV-RFP) into the other target (**Fig. 1A**). Then we examined the proportion of the double-labeled yellow neurons out of all labeled neurons in the VP (**Fig. 1B**). Our data show that overlap between projections ranged between 7-20%, with the $VP_{\rightarrow LH}$ projections showing the lowest overlap proportions and especially low overlap with $VP_{\rightarrow VTA}$ projections (7%) (**Fig. 1C**). This may be surprising, as a previous study[28] showed that most of the VP projection neurons, regardless of their final target, pass through the LH, but another study showed different behavioral effects for $VP_{\rightarrow LH}$ and $VP_{\rightarrow VTA}$ projections[11]. It is possible that the levels of overlap between VP projections reported here are underestimations as the overlap may be affected by the efficiency of virus uptake by axons and by microinjection localization.

### *Distinct molecular signatures within VP projection neurons*

Given that the projections of the VP originate in largely distinct sets of neurons, we aimed to examine whether these sets of VP projection neurons exhibit distinct profiles at the molecular level. Although studies have identified the neurochemical composition of VP projection neurons using *in situ* hybridization[8,9,29], we profiled global translatome-wide signatures within VP projection neurons. This allows us to identify patterns and novel genes enriched within VP projection neurons.To this end, gene expression profiles of VP projection neurons were assessed using RNA-sequencing (**Fig. 2A**). Retrograde Cre virus (AAV5-Cre) was infused either into the VTA, LHb, LH, MDT or VP. This resulted in Cre-dependent expression of HA-tagged ribosomal protein within upstream VP neurons. Infusion of AAV5-Cre directly into the VP served as a comparison of non-pathway specific

VP (global VP) gene expression. VP tissue was collected from mice and Ribotag methods were used to isolate pathway-specific ribosome-associated mRNA from VP neurons. RNA-sequencing libraries were constructed from each VP projection group and followed by translatome profiling (**Fig. 2A**).

First, pair-wise comparisons of gene expression patterns from $VP_{\rightarrow VTA}$, $VP_{\rightarrow LHb}$, $VP_{\rightarrow LH}$ and $VP_{\rightarrow MDT}$ were compared to gene expression within non-projection specific VP neurons (**Fig. 2B**). The following number of differentially expressed genes (DEGs) were detected in each VP projection neuron: $VP_{\rightarrow MDT}$: 4318; $VP_{\rightarrow VTA}$: 1982; $VP_{\rightarrow LHb}$:1709 and $VP_{\rightarrow LH}$: 1308. To further characterize global gene expression patterns, we performed Rank-Rank Hypergeometric Overlap (RRHO) analysis[30], which compares gene expression between two lists in a threshold-free manner. Heat maps display overlap at those points, determined by relative effect sizes in differential gene expression using -$\log_{10}$(p-value). Comparisons between gene expression lists of all six possible pairs of VP projections were performed (**Fig. 2C**). High concordance is seen within genes upregulated within $VP_{\rightarrow LH}$ versus $VP_{\rightarrow MDT}$ in relation to VP global neurons (peak: -$\log_{10}$(p-value): 541) and $VP_{\rightarrow LHb}$ versus $VP_{\rightarrow MDT}$ (peak: -$\log_{10}$(p-value): 334). High concordance is also observed within downregulated genes in $VP_{\rightarrow VTA}$ versus $VP_{\rightarrow LH}$ neurons (peak: -$\log_{10}$(p-value): 393). These data overall suggest that $VP_{\rightarrow MDT}$ has the highest number of upregulated genes and exhibits the highest overlap of upregulated gene expression patterns among other VP projection neuron types.

To identify cell-type specific molecules and processes, additional analysis was performed on genes upregulated (i.e. enriched) within the VP projections. $VP_{\rightarrow MDT}$ neurons had the highest number of upregulated DEGs (708) in comparison to other VP neuron types ($VP_{\rightarrow VTA}$: 489; $VP_{\rightarrow LH}$: 454; $VP_{\rightarrow LHb}$: 402). Upregulated genes were largely distinct from one another (**Fig. 3A**), with only 66 upregulated genes shared amongst all VP neuron types. Consistent with the patterns detected from RRHO analysis, $VP_{\rightarrow MDT}$ and $VP_{\rightarrow LH}$ projection neurons shared the highest number of upregulated genes (267 total) and $VP_{\rightarrow LH}$ and $VP_{\rightarrow LHb}$ have little gene overlap (133 total). To characterize the biological processes and cellular functions associated with genes enriched within each VP neuronal type, gene ontology (GO) analysis was performed (**Fig. 3B**). All projection neuron types have enrichment for GABA receptor activity processes, suggesting that all these neuronal types receive GABAergic inputs. $VP_{\rightarrow VTA}$ neurons have genes enriched for glutamate receptor activity and $VP_{\rightarrow LHb}$ neurons are enriched for dopamine binding, which were not detected

in other projection neuron types. Interestingly, shared GO terms across VP projection types include synaptic transmission and cytoskeletal protein binding. This may indicate that VP projection neurons express distinct sets of genes to regulate processes for synaptic communication. Similarly, GO terms for metabolic process and mitochondrion organization are detected amongst $VP_{\rightarrow VTA}$ and $VP_{\rightarrow MDT}$ neurons. This suggests that neuronal types may have distinct molecules that regulate mitochondrial and energy processes. Overall, the enriched genes and biological processes within each projection neuron type may underlie the VP projection-specific functions and responses.

***Different input patterns for different VP projections***

The four VP projections we test here differ, by definition, in the target they project to. However, they may also receive their inputs from different sources, thus generating parallel segregated circuits. To test whether the VP projections differ in their input patterns we used the Testing the Relationship between Input and Output (TRIO) method[13], which allows labeling of monosynaptic inputs to a specific projection neuron (**Fig. 4A**). We first injected a retrograde virus encoding Cre recombinase (rAAV-Cre) into either of the four VP targets (i.e. VTA, LH, MDT or LHb) and then viruses that encode for the TVA receptor and the rabies glycoprotein in a Cre-dependent manner into the VP. Thus, only VP neurons projecting to the site injected with the rAAV-Cre would express the TVA receptor and the rabies glycoprotein ("starter cells", **Supplementary Figure 1**). Lastly, we injected the modified rabies virus[31] into the VP and tested neuron labeling using the iDisco+ method[32] and light sheet fluorescence microscopy (**Fig. 4A,B**).

Our data show that although all four VP projections receive input from largely the same sources, they differ in the relative contribution of each input (**Fig. 4C,D; Supplementary Table 3**). The main inputs to all VP projections originated in the hypothalamus, striatum, amygdala and olfactory areas, with lesser contribution from the midbrain, hippocampus and cortex.

Some inputs were more pronounced on specific projections (**Fig. 4D**). For example, hypothalamic inputs were less dominant in $VP_{\rightarrow LHb}$ neurons while olfactory inputs were significantly stronger on $VP_{\rightarrow LH}$ projections and striatal inputs (mainly from the NAc) were specifically enriched in $VP_{\rightarrow VTA}$ projections. Interestingly, the $VP_{\rightarrow LH}$ and $VP_{\rightarrow VTA}$ projections, that show minimal overlap (**Fig. 1C**), also show various differences in their

inputs, the $VP_{\rightarrow LH}$ projections recivieng more olfactory and less striatal and amygdalar inputs compared to $VP_{\rightarrow VTA}$ projections.

**The $VP_{\rightarrow MDT}$ projection receives less inhibitory input compared to the other VP projections**

The projections of the VP may differ not only in their gene expression (**Figs. 2,3**) or their input patterns (**Fig. 4**) but also in the characteristics of the synaptic inputs they receive. To examine this, we used the whole-cell patch clamp technique and recorded from each of the four VP projections the evoked input from the NAc and the global spontaneous inputs they receive (**Fig. 5**).

Examination of the evoked NAc input to each of the VP projections tested here revealed no difference between the projections. In all projections tested, the proportion of neurons in which we detected evoked NAc input was similar (between 66-77 %, **Fig. 5A-B**) and the average amplitude of the optogenetically-evoked inhibitory postsynaptic current (oIPSC) was similar (**Fig. 5C**). This was also true for the paired pulse ratio (PPR) and coefficient of variation of the evoked currents (two measures reflecting the probability of release[33,34]) (**Fig. 5D-E**). Lastly, in all VP projections application of picrotoxin completely abolished the NAc oIPSC (**Fig. 5F**), indicating a GABAergic synapse.

Comparing the characteristics of the spontaneous postsynaptic currents (sPSCs) between the projections revealed that while they do not differ in the amplitude of the sPSCs (**Fig. 5G**), the $VP_{\rightarrow MDT}$ projection shows a significantly lower frequency of sPSCs compared to the other projections (**Fig. 5H**). This difference may be due to less GABAergic input because when we washed the slices with picrotoxin (100 μM), a GABA-A receptor antagonist, the reduction in the frequency of sPSCs was significantly smaller in $VP_{\rightarrow MDT}$ neurons (52.8±33 % reduction) (**Fig. 5I-J**).

***$VP_{\rightarrow LH}$ neurons are more excitable and $VP_{\rightarrow VTA}$ neurons are less excitable than the average VP neuron***

We next tested various properties that contribute to the excitability of the VP projection neurons (**Fig. 6A**). The resting membrane potential (**Fig. 6B**) did not differ between VP projections and ranged between -45.8 mV and -47.2 mV on average. In contrast, the firing rate at rest (**Fig. 6C-D**) did differ between projections. In particular, the $VP_{\rightarrow LH}$ neurons

had the highest firing rate (10.9±8.1 Hz), which was significantly higher than the firing rate of $VP_{\rightarrow MDT}$ (6.1±4.8 Hz) and $VP_{\rightarrow VTA}$ neurons (6.5±5.2 Hz).

When we applied a series of depolarizing current steps to the VP projections (**Fig. 6E-G**), we found that the projections differed both in the number of action potentials they generated per step and in the latency to the first action potential. Note that the $VP_{\rightarrow LH}$ projections, who had the highest firing rates at rest (**Fig. 6C**), also showed strong firing and quick response when depolarized.

To evaluate the average excitability of the projections we generated an "excitability index". In each of the measured parameters we pooled all cells together and applied z-scores to all cells. Thus, each neuron had four z-scores (one from each experiment) and the excitability index of a neuron is the average of its four z-scores. Comparison of the excitability indexes between VP projections (**Fig. 6H**) demonstrated that it differed between projections and that the $VP_{\rightarrow LH}$ and $VP_{\rightarrow VTA}$ projections had significantly different excitability indexes, 0.25 and -0.21, respectively. Moreover, when comparing the excitability indexes to zero, which reflects the average excitability of a VP neuron, the average excitability index of the $VP_{\rightarrow LH}$ neurons was significantly higher than zero while that of $VP_{\rightarrow VTA}$ neurons was significantly lower than zero. Thus, our data suggest that $VP_{\rightarrow LH}$ neurons are a subtype of VP neurons that is more excitable than the average VP neuron while $VP_{\rightarrow VTA}$ neurons are a differen subtype of VP neurons that is less excitable than the average VP neuron. This, together with our anatomical findings (**Figs. 1,4**), strengthens the hypothesis that $VP_{\rightarrow LH}$ and $VP_{\rightarrow VTA}$ neurons are largely different subpopulations.

**Genes critical for ion transport enriched within $VP_{\rightarrow LH}$ and $VP_{\rightarrow VTA}$ neurons**

To identify potential molecules underlying neuronal responses seen between $VP_{\rightarrow VTA}$ and $VP_{\rightarrow LH}$ neurons, we compared genes enriched within both VP projection neuron types. We found 156 genes enriched within both $VP_{\rightarrow LH}$ and $VP_{\rightarrow VTA}$ neurons (**Fig. 7A**). GO Term analysis illustrated that the 156 genes belonged to processes related to neuron development, synaptic transmission, GABA signaling pathways, chromatin assembly and ion transport (**Fig. 7B**). This is consistent with previous work identifying VP GABAergic projections to the LH and VTA[9,11]. It also suggests that despite electrophysiological differences, there may be shared molecules that regulate presynaptic and synaptic processes between $VP_{\rightarrow LH}$ and $VP_{\rightarrow VTA}$ neurons. Given the differences in

excitability between these projection neurons, we focused our analysis on genes associated with ion transport, which includes genes encoding subunits of ion channels and transporters. A heat map shows the genes enriched for ion transport within each projection type and their log-fold changes in comparison to global VP neuron gene expression. Among the genes enriched in both $VP_{\rightarrow LH}$ and $VP_{\rightarrow VTA}$ neurons, *GABRA5*, the GABA-A receptor alpha 5 subunit, is the highest expressing gene. A predicted transcription analysis on the genes associated with ion transport highlights RFX3 as a top predictor regulator of several shared ion transport genes. This presents a possible target for shared ion genes within $VP_{\rightarrow VTA}$ and $VP_{\rightarrow LH}$ neurons.

To identify genes and biological processes distinct to each neuronal type, GO term analysis was performed on the unshared genes within $VP_{\rightarrow LH}$ (298 genes) and $VP_{\rightarrow VTA}$ (333 genes) neurons. Interestingly, both sets of genes were associated with processes related to synaptic transmission and ion transport but also show intriguing differences that may contrtibute to the differences in excitability (**Fig. 7C,D**). For example, both neuron types have enriched expression of potassium chanels, despite distinct families expressed within each neuronal type. $VP_{\rightarrow LH}$ neurons show increased expression of channels from the $K_v3$ family (*KCNC1, KCNC2*) while $VP_{\rightarrow VTA}$ neurons show increasd expression of other potassium channel subtypes (*KCND2, KCNAB1)*. Since $K_v3$ channels are known to be important for high-frequency firing[35–37], the increased expression of *KCNC1,2* in $VP_{\rightarrow LH}$ neurons may underlie their higher excitability.

Predicted transcription factor analysis was performed on synaptic genes enriched within $VP_{\rightarrow LH}$ neurons and $VP_{\rightarrow VTA}$ neurons. We found that RNF138 was a top predicted regulator for a subset of $VP_{\rightarrow LH}$ ion transport genes, and DLX4 was a top predicted regulator for a subset of ion transport genes within $VP_{\rightarrow VTA}$ neurons. Altogether, these data demonstrate that $VP_{\rightarrow VTA}$ and $VP_{\rightarrow LH}$ neurons have sets of ion transport genes that are enriched within each projection neuron type and present novel molecular targets to study VP projection-specific neuronal function.

### *Opposite roles for $VP_{\rightarrow LH}$ and $VP_{\rightarrow VTA}$ projections in cocaine conditioned place preference*

Our data so far indicates different VP projections show different characteristics in many aspects. In particular, the $VP_{\rightarrow LH}$ and $VP_{\rightarrow VTA}$ projections emerge as largely separate

neuronal populations (**Fig. 1**) with different input patterns (**Fig. 4**), different gene expression (**Fig. 7**) and contrasting physiological properties (**Fig. 6**). In light of these differences between the projections, we next tested whether these projections affect differently the motivation to receive drug reward after abstinence in a cocaine conditioned place preference (CPP) procedure.

To inhibit the activity of a specific projection (e.g. $VP_{\rightarrow LH}$) we injected a retrograde AAV encoding for Cre recombinase (rAAV-Cre) in the target area to express Cre in the specific VP projection neurons and expressed the inhibitory version of the Designer Receptor Exclusively Activated by Designer Drugs (DREADDs) in a cre-dependent manner in the VP (AAV-DIO-hM4Di-GFP) (control mice were injected with a sham virus, AAV-DIO-eYFP) (**Fig. 8A**). We then trained mice to associate one side of the CPP box with cocaine using the cocaine CPP paradigm (**Fig. 8B**, see Methods) and then allowed them to undergo abstinence in their home cages for 14 days. Thirty minutes before the CPP test, we injected all mice with CNO (3 mg/kg, i.p.) and then tested their preference to the cocaine-paired side.

Our data show that inhibiting the different VP projections had different effects on the preference of the cocaine paired side (**Fig. 8C-H**). In particular, the average CPP score when inhibiting the $VP_{\rightarrow LH}$ projection (0.34±0.19) was significantly lower than the CPP score when inhibiting the $VP_{\rightarrow VTA}$ (0.63±0.10) or $VP_{\rightarrow MDT}$ (0.61±0.15) projections. Comparison of the CPP scores to that of the control group (injected with CNO but expressing the sham virus, average CPP score of 0.51) revealed that inhibiting the $VP_{\rightarrow LH}$ projection significantly reduced the CPP score while inhibiting the $VP_{\rightarrow VTA}$ projection significantly increased the CPP score. Inhibiting the $VP_{\rightarrow MDT}$ or $VP_{\rightarrow LHb}$ projections did not affect the CPP score. Inhibiting the different projections did not change differently the overall locomotion of the mice (**Fig. 8I**). Thus, our data demonstrates that different VP projections have different roles in renewal of cocaine CPP after abstinence, and highlight the different, and maybe opposite roles of $VP_{\rightarrow LH}$ and $VP_{\rightarrow VTA}$ in cocaine preference.

## Discussion

The VP is a structure largely composed of GABAergic neurons and has numerous downstream projection targets. It has been assumed that the cellular composition of the

different projections is largely similar, despite the VP's projection-specific roles in behavior. In this manuscript we provide for the first time a thorough examination of four major outputs of the VP and compare directly their genetic profile, input sources, physiological characteristics and roles in cocaine motivation after withdrawal. We find that the different VP projections show distinct characteristics in all properties examined. Each projection has distinct sets of enriched genes (**Figs. 2-3**), receives different patterns of inputs from various regions of the brain (**Fig. 4**), exhibits different levels of excitability and inhibitory input (**Figs. 5-6**) and has differential roles in regulating cocaine CPP behavior after abstinence (**Fig. 8**). In particular, the VP projections to the LH and VTA stand out as being largely distinct cell populations. They show a minimal level of projection overlap (**Fig. 2**), differences in input sources (**Fig. 4**), express different sets of enriched genes (**Fig. 7**), have different excitability levels (**Fig. 6**) and show opposite effects on cocaine CPP (**Fig. 8**).

VP heterogeneity

Our data suggest that the four projection neurons of the VP examined here differ from each other in multiple aspects, potentially suggesting some of these projections contain distinct subtypes of VP neurons. This supports previous studies attributing different behavioral roles to distinict VP outputs[5,8,11,29,38,39]. Out of the projections examined here, the $VP_{\rightarrow LH}$ neurons have the lowest overlap with other VP projection neurons, show enrichment of genes critical for axogenesis and GABAergic receptors and are hyperexcitable. This suggests that $VP_{\rightarrow LH}$ neurons are a distinct subgroup of neurons that are potentially poised to propagate information quickly from their inputs. In addition, $VP_{\rightarrow VTA}$ and $VP_{\rightarrow LHb}$ neurons are enriched for biological processes distinct from other VP projection neurons ($VP_{\rightarrow VTA}$ : Glutamate receptor activity; $VP_{\rightarrow LHb}$: dopamine binding activity) suggesting these neuronal types may have distinct inputs from other VP projection neurons.

Unlike $VP_{\rightarrow LH}$ neurons, $VP_{\rightarrow MDT}$ neurons show an average level of excitability, have the largest proportion of double-labeling with other VP projections and display large overlap of gene expression patterns with other VP projection neuron types. Despite the similarity to other VP projections, $VP_{\rightarrow MDT}$ neurons are distinct in their low inhibitory input (**Fig. 5**). This relatively weak inhibition of $VP_{\rightarrow MDT}$ neurons may stem from the small proportion of inputs from the striatum (**Fig. 4**). Thus, a group of neurons may be similar to other neurons

in one aspect but different in other aspects, calling for multimodal characterization of neuronal subtypes.

One of the major inputs to the VP is inhibitory input from the NAc. Our data show that about 75% of the neurons in the VP indeed receive synaptic inhibitory input from the NAc (**Fig. 5**), similar to estimations in previous studies[40,41]. Our GO term analysis could reflect this, as all VP projection neurons have genes enriched for GABA receptor activity. Nevertheless, our viral tracing experiments show that more striatal neurons converge on $VP_{\rightarrow VTA}$ neurons than on $VP_{\rightarrow LH}$ or $VP_{\rightarrow MDT}$ neurons (**Fig. 4**). It is possible that exposure to reward may change the innervation pattern of the VP by the NAc, as we and others have previously observed synaptic adaptations in VP neurons after exposure to cocaine or highly-palatable food[24,25,41–43]. Our data overall suggests that VP projection neurons, with the exception of $VP_{\rightarrow MDT}$ neurons, are largely non-overlapping and composed of distinct genetic and cellular profiles. These findings also highlight the need to further interrogate how the VP encodes distinct sets of information from its various inputs to promote stimuli and input-specific behaviors.

<u>The difference between $VP_{\rightarrow LH}$ and $VP_{\rightarrow VTA}$ projections</u>

Our results highlight the $VP_{\rightarrow LH}$ and the $VP_{\rightarrow VTA}$ projections as being particularly distinct from each other. They show only 7% overlap (**Fig. 1**) and a large number of upregulated genes within these populations are non-overlapping (**Fig. 7**). We also detected differences in excitability, with $VP_{\rightarrow LH}$ neurons being more excitable than $VP_{\rightarrow VTA}$ neurons (**Fig. 6**), possibly due to specific upregulation of genes encoding for the $K_v3$ potassium channel family, known to allow high firing frequencies[35–37] (**Fig. 7**). Consistent with this, chemogenetic inhibition of these populations resulted in opposite behavioral effects; inhibition of $VP_{\rightarrow LH}$ neurons decreases while inhibition of $VP_{\rightarrow VTA}$ neurons increases cocaine CPP.

The differences we report on $VP_{\rightarrow LH}$ and $VP_{\rightarrow VTA}$ neurons challenge several previous notions of the VP. First, an anatomical study suggests that approximately 90% of VP projections, including those to the VTA, pass through the LH[28]. In fact, the LH is positioned between the VP and the VTA[44]. Our data suggest that the $VP_{\rightarrow VTA}$ projections do not collateralize to the LH, and are strictly passing through the structure. Our CPP work does demonstrate that the VP exerts projection-specific effects on behavior, as previously

seen[5,8,9,45]. However, there is conflicting reports on the effects of inhibiting VP projection neurons on drug seeking. These differences may be due to different cell-type specific manipulations, as Prasad et al. had found that inhibition of $VP_{\rightarrow LH}$ GABAergic neurons, but not $VP_{\rightarrow LH}$ parvalbumin-expressing neurons reduces renewal of operant-based alcohol seeking in rats[11]. This may also be due to species-specific effects, as inhibition of $VP_{\rightarrow VTA}$ neurons has previously been shown to enhance cocaine seeking in mice[5], but impair cocaine-seeking in rats[46]. Alternatively, it is possible that different circuits and cell-types are affected due to extinction training[11,46] and forced abstinence[5]. Further investigation into these underlying differences is required to better understand the role of VP in drug-seeking.

The mechanism allowing the $VP_{\rightarrow LH}$ and the $VP_{\rightarrow VTA}$ projections to have different behavioral roles in drug reward after abstinence is still not understood. One possibility is potential opposite effects on dopamine release from VTA neurons. $VP_{\rightarrow VTA}$ neurons target both GABA and dopamine neurons[25,47,48]. It is still not known how activation of VP input to the VTA affects dopamine levels but it is plausible that it enhances dopamine release as it increases the firing rate of putative dopamine neurons[46]. LH GABAergic neurons that project to the VTA increase firing of VTA dopamine neurons[49]. These neurons are also a main target of $VP_{\rightarrow LH}$ projections[50]. Thus, activation of $VP_{\rightarrow LH}$ neurons, which are mostly GABAergic[1], may result in a net decrease in dopamine release. Therefore, $VP_{\rightarrow VTA}$ and $VP_{\rightarrow LH}$ are expected to have opposite effects on dopamine release from the VTA. This may underlie their opposite effect on cocaine CPP.

Altogether, our multimodal interrogartion of the VP demonstrates that VP projection neurons have relatively distinct pathways, cellular properties and molecular compositions. These baseline differences may reflect their projection-specific roles of cocaine-related behaviors. Our behavioral findings illustrate how VP projection neurons have differential roles of in cocaine reward, which is consistent with previous work in the field. This work emphasizes the importance in further investigating and characterizing the VP projections and cell types in addiction processes.

**Acknowledgements**

This study was supported by the U.S.-Israel Binational Science Foundation (grants 2015239 and 2017252 to YMK and MKL) and the Israeli Science Foundation (Grant No. 1381/15 to YMK).

Bibliography


1 Kupchik YM, Prasad AA. Ventral pallidum cellular and pathway specificity in drug seeking. *Neurosci Biobehav Rev* 2021; **131**: 373–386.

2 Root DH, Melendez RI, Zaborszky L, Napier TC. The ventral pallidum: Subregion-specific functional anatomy and roles in motivated behaviors. *Prog Neurobiol* 2015; **130**: 29–70.

3 Smith KS, Tindell AJ, Aldridge JW, Berridge KC. Ventral pallidum roles in reward and motivation. *Behav Brain Res* 2009; **196**: 155–167.

4 Heinsbroek JA, Bobadilla A-C, Dereschewitz E, Assali A, Chalhoub RM, Cowan CW *et al.* Opposing regulation of cocaine seeking by glutamate and GABA neurons in the ventral pallidum. *Cell Rep* 2020; **30**: 2018–2027.e3.

5 Pribiag H, Shin S, Wang EH-J, Sun F, Datta P, Okamoto A *et al.* Ventral pallidum DRD3 potentiates a pallido-habenular circuit driving accumbal dopamine release and cocaine seeking. *Neuron* 2021; **109**: 2165–2182.e10.

6 McKenna JT, Yang C, Franciosi S, Winston S, Abarr KK, Rigby MS *et al.* Distribution and intrinsic membrane properties of basal forebrain GABAergic and parvalbumin neurons in the mouse. *J Comp Neurol* 2013; **521**: 1225–1250.

7 Zaborszky L, Buhl DL, Pobalashingham S, Bjaalie JG, Nadasdy Z. Three-dimensional chemoarchitecture of the basal forebrain: spatially specific association of cholinergic and calcium binding protein-containing neurons. *Neuroscience* 2005; **136**: 697–713.

8 Tooley J, Marconi L, Alipio JB, Matikainen-Ankney B, Georgiou P, Kravitz AV *et al.* Glutamatergic Ventral Pallidal Neurons Modulate Activity of the Habenula-Tegmental Circuitry and Constrain Reward Seeking. *Biol Psychiatry* 2018; **83**: 1012–1023.

9 Faget L, Zell V, Souter E, McPherson A, Ressler R, Gutierrez-Reed N *et al.* Opponent control of behavioral reinforcement by inhibitory and excitatory projections from the ventral pallidum. *Nat Commun* 2018; **9**: 849.

10 Floresco SB, Braaksma DN, Phillips AG. Involvement of the ventral pallidum in working memory tasks with or without a delay. *Ann N Y Acad Sci* 1999; **877**: 711–716.

11 Prasad AA, Xie C, Chaichim C, Nguyen JH, McClusky HE, Killcross S *et al.* Complementary roles for ventral pallidum cell types and their projections in relapse. *J Neurosci* 2020; **40**: 880–893.

12 Khan HA, Urstadt KR, Mostovoi NA, Berridge KC. Mapping excessive “disgust” in the brain: Ventral pallidum inactivation recruits distributed circuitry to make

sweetness “disgusting”. *Cogn Affect Behav Neurosci* 2020; **20**: 141–159.

13 Schwarz LA, Miyamichi K, Gao XJ, Beier KT, Weissbourd B, DeLoach KE *et al.* Viral-genetic tracing of the input-output organization of a central noradrenaline circuit. *Nature* 2015; **524**: 88–92.

14 Wickersham IR, Finke S, Conzelmann K-K, Callaway EM. Retrograde neuronal tracing with a deletion-mutant rabies virus. *Nat Methods* 2007; **4**: 47–49.

15 Habib N, Avraham-Davidi I, Basu A, Burks T, Shekhar K, Hofree M *et al.* Massively parallel single-nucleus RNA-seq with DroNc-seq. *Nat Methods* 2017; **14**: 955–958.

16 Kim CK, Adhikari A, Deisseroth K. Integration of optogenetics with complementary methodologies in systems neuroscience. *Nat Rev Neurosci* 2017; **18**: 222–235.

17 Rost BR, Wietek J, Yizhar O, Schmitz D. Optogenetics at the presynapse. *Nat Neurosci* 2022; **25**: 984–998.

18 Mardinly AR, Oldenburg IA, Pégard NC, Sridharan S, Lyall EH, Chesnov K *et al.* Precise multimodal optical control of neural ensemble activity. *Nat Neurosci* 2018; **21**: 881–893.

19 Roth BL. DREADDs for neuroscientists. *Neuron* 2016; **89**: 683–694.

20 BRAIN Initiative Cell Census Network (BICCN). A multimodal cell census and atlas of the mammalian primary motor cortex. *Nature* 2021; **598**: 86–102.

21 Wang Y, Krabbe S, Eddison M, Henry FE, Fleishman G, Lemire AL *et al.* Multimodal mapping of cell types and projections in the central nucleus of the amygdala. *BioRxiv* 2022. doi:10.1101/2022.10.19.512845.

22 Engeln M, Song Y, Chandra R, La A, Fox ME, Evans B *et al.* Individual differences in stereotypy and neuron subtype translatome with TrkB deletion. *Mol Psychiatry* 2021; **26**: 1846–1859.

23 Chandra R, Francis TC, Konkalmatt P, Amgalan A, Gancarz AM, Dietz DM *et al.* Opposing role for Egr3 in nucleus accumbens cell subtypes in cocaine action. *J Neurosci* 2015; **35**: 7927–7937.

24 Inbar K, Levi LA, Bernat N, Odesser T, Inbar D, Kupchik YM. Cocaine Dysregulates Dynorphin Modulation of Inhibitory Neurotransmission in the Ventral Pallidum in a Cell-Type-Specific Manner. *J Neurosci* 2020; **40**: 1321–1331.

25 Levi LA, Inbar K, Nachshon N, Bernat N, Gatterer A, Inbar D *et al.* Projection-Specific Potentiation of Ventral Pallidal Glutamatergic Outputs after Abstinence from Cocaine. *J Neurosci* 2020; **40**: 1276–1285.

26 Gendelis S, Inbar D, Inbar K, Mesner S, Kupchik YM. Metaplasticity in the Ventral Pallidum as a Potential Marker for the Propensity to Gain Weight in Chronic High-Calorie Diet. *J Neurosci* 2020; **40**: 9725–9735.

27 Ben-Shaul Y. OptiMouse: a comprehensive open source program for reliable detection and analysis of mouse body and nose positions. *BMC Biol* 2017; **15**: 41.

28 Tripathi A, Prensa L, Mengual E. Axonal branching patterns of ventral pallidal neurons in the rat. *Brain Struct Funct* 2013; **218**: 1133–1157.

29 Vachez YM, Tooley JR, Abiraman K, Matikainen-Ankney B, Casey E, Earnest T *et al.* Ventral arkypallidal neurons inhibit accumbal firing to promote reward consumption. *Nat Neurosci* 2021; **24**: 379–390.

30 Plaisier SB, Taschereau R, Wong JA, Graeber TG. Rank-rank hypergeometric overlap: identification of statistically significant overlap between gene-expression signatures. *Nucleic Acids Res* 2010; **38**: e169.

31 Osakada F, Callaway EM. Design and generation of recombinant rabies virus vectors. *Nat Protoc* 2013; **8**: 1583–1601.

32 Renier N, Wu Z, Simon DJ, Yang J, Ariel P, Tessier-Lavigne M. iDISCO: a simple, rapid method to immunolabel large tissue samples for volume imaging. *Cell* 2014; **159**: 896–910.

33 Berninger B, Schinder AF, Poo MM. Synaptic reliability correlates with reduced susceptibility to synaptic potentiation by brain-derived neurotrophic factor. *Learn Mem* 1999; **6**: 232–242.

34 Schinder AF, Berninger B, Poo M. Postsynaptic target specificity of neurotrophin-induced presynaptic potentiation. *Neuron* 2000; **25**: 151–163.

35 Kaczmarek LK, Zhang Y. Kv3 channels: enablers of rapid firing, neurotransmitter release, and neuronal endurance. *Physiol Rev* 2017; **97**: 1431–1468.

36 Rudy B, McBain CJ. Kv3 channels: voltage-gated K+ channels designed for high-frequency repetitive firing. *Trends Neurosci* 2001; **24**: 517–526.

37 Lien C-C, Jonas P. Kv3 potassium conductance is necessary and kinetically optimized for high-frequency action potential generation in hippocampal interneurons. *J Neurosci* 2003; **23**: 2058–2068.

38 Leung BK, Balleine BW. Ventral pallidal projections to mediodorsal thalamus and ventral tegmental area play distinct roles in outcome-specific Pavlovian-instrumental transfer. *J Neurosci* 2015; **35**: 4953–4964.

39 Engeln M, Fox ME, Chandra R, Choi EY, Nam H, Qadir H *et al.* Transcriptome profiling of the ventral pallidum reveals a role for pallido-thalamic neurons in cocaine reward. *Mol Psychiatry* 2022. doi:10.1038/s41380-022-01668-7.

40 Kupchik YM, Brown RM, Heinsbroek JA, Lobo MK, Schwartz DJ, Kalivas PW. Coding the direct/indirect pathways by D1 and D2 receptors is not valid for accumbens projections. *Nat Neurosci* 2015; **18**: 1230–1232.

41 Creed M, Ntamati NR, Chandra R, Lobo MK, Lüscher C. Convergence of reinforcing and anhedonic cocaine effects in the ventral pallidum. *Neuron* 2016; **92**: 214–226.

42 Gendelis S, Inbar D, Inbar K, Mesner S, Kupchik YM. Metaplasticity in the ventral pallidum as a potential marker for the development of diet-induced obesity. *BioRxiv* 2020. doi:10.1101/2020.03.09.983114.

43 Matsui A, Alvarez VA. Cocaine Inhibition of Synaptic Transmission in the Ventral Pallidum Is Pathway-Specific and Mediated by Serotonin. *Cell Rep* 2018; **23**: 3852–3863.

44 Paxinos G, Franklin KBJ. *The Mouse Brain in Stereotaxic Coordinates*. 2nd ed. Academic Press: San Diego, CA, USA, 2001.

45 Prasad AA, McNally GP. Ventral Pallidum Output Pathways in Context-Induced Reinstatement of Alcohol Seeking. *J Neurosci* 2016; **36**: 11716–11726.

46 Mahler SV, Vazey EM, Beckley JT, Keistler CR, McGlinchey EM, Kaufling J *et al.* Designer receptors show role for ventral pallidum input to ventral tegmental area in cocaine seeking. *Nat Neurosci* 2014; **17**: 577–585.

47 Hjelmstad GO, Xia Y, Margolis EB, Fields HL. Opioid modulation of ventral pallidal afferents to ventral tegmental area neurons. *J Neurosci* 2013; **33**: 6454–6459.

48 Watabe-Uchida M, Zhu L, Ogawa SK, Vamanrao A, Uchida N. Whole-brain mapping of direct inputs to midbrain dopamine neurons. *Neuron* 2012; **74**: 858–873.

49 Nieh EH, Vander Weele CM, Matthews GA, Presbrey KN, Wichmann R, Leppla CA *et al.* Inhibitory Input from the Lateral Hypothalamus to the Ventral Tegmental Area Disinhibits Dopamine Neurons and Promotes Behavioral Activation. *Neuron* 2016; **90**: 1286–1298.

50 Jennings JH, Rizzi G, Stamatakis AM, Ung RL, Stuber GD. The inhibitory circuit architecture of the lateral hypothalamus orchestrates feeding. *Science* 2013; **341**: 1517–1521.

## Figures

**Figure 1 – Minimal overlap between ventral pallidal projections to the MDT, LHb, LH and VTA.** (**A**) Experimental setup. We injected each mouse with two retrograde viruses expressing either RFP (rAAV-RFP) or GFP (rAAV-GFP), each in a different target of the VP. Thus, we could identify neurons projecting to either target and those projecting to both. (**B**) Sample images of labeled $VP_{\rightarrow MDT}$ neurons, $VP_{\rightarrow LH}$ neurons and double-labeled neurons projecting to both targets. (**C**) Pie charts depicting for each pair of VP targets the proportion of double-labeled VP neurons projecting to both targets out of all labeled neurons (arranged from lowest to highest proportion of double-labeled neurons). The proportion of VP neurons projecting to both targets tested was in the range of 7-20%. Note that $VP_{\rightarrow LH}$ neurons showed the lowest proportions of overlap, especially with $VP_{\rightarrow VTA}$ neurons.

**Figure 2- VP projection neurons have distinct molecular signatures.** (**A**) Retrograde Cre (AAV5-Cre) was infused into 1 of 4 downstream VP regions (MDT; LHb;LH;VTA) or VP within Ribotag male mice (n=16 mice per projection). HA-immunoprecipitation procedures were employed to isolate RNA from distinct VP projection neurons or all VP neurons. RNA-sequencing libraries were generated and analyzed from these samples to characterize baseline gene expression profiles within VP neurons projecting to the MDT, LHb, LH, VTA. (**B**) Differential Gene Expression (DEG) analysis was generated by comparing gene expression within specific VP projection neuron types relative to the global VP gene expression (uncorrected $p<0.05$). Transcriptional patterns within each VP projection neuron type are shown in a heat map. (**C**) Rank-Rank Hypergeometric Overlap (RRHO) analysis comparing gene expression in a threshold free manner suggests $VP_{\rightarrow MDT}/VP_{\rightarrow LH}$ and $VP_{\rightarrow MDT}/VP_{\rightarrow LHb}$ projection neurons have the highest concordance of gene expression patterns.

**Figure 3 - Gene ontology analysis identifies biological processes and molecular functions enriched within VP projection neurons.** (**A**) Genes upregulated within each VP projection neuron type were compared in Venn diagrams. The $VP_{\rightarrow MDT}$ projection neuron has the highest number of enriched genes, with $VP_{\rightarrow MDT}$ and $VP_{\rightarrow LH}$ sharing the highest number of enriched genes. (**B**) Top Gene Ontology (GO) terms enriched in upregulated genes from each VP projection neuron.

**Figure 4 – Distinct monosynaptic input patterns between different ventral pallidal projections.** (**A**) To visualize the monosynaptic inputs to each ventral pallidum projection we injected a retrograde virus expressing Cre (rAAV-Cre) into one of the

targets of the VP and the rabies helper viruses expressing in a cre-dependent manner the avian tumor receptor A (AAV-FLEx-TVA) and the rabies glycoprotein (AAV-FLEx-G) into the VP. Fourteen days later we injected the pseudotyped rabies virus (RV*d*G) into the VP to label all monosynapic inputs to a certain VP projection. We then cleared the brains with iDisco+ and imaged the cleared brains with light sheet fluorescence microscopy (LSFM). (**B**) Top - LSFM image of labeled neurons in the NAc. Bottom – magnification of the neuron marked by a dotted square in the top image. (**C**) Proportions of the major inputs to the four VP projections. Colored ring surrounding pie charts indicates grouping of subparts of the same brain region into the regions used in panel (D). Although the four VP projections receive input from the same brain regions, the proportions of each input vary between the projections. (**D**) The proportions of specific inputs between the four VP projections are significantly different (Two-way ANOVA, main effect for input source, $F_{(9,80)}=23.8$, $p<0.0001$; interaction (input source X VP projection) effect, $F_{(27,80)}=3.42$, $p<0.0001$). The $VP_{\rightarrow LH}$ projections show several differences from the $VP_{\rightarrow VTA}$ projections, including stronger olfactory input (Tukey's multiple comparison test ($p<0.0001$) but weaker striatal ($p=0.016$) and amygdalar ($p=0.006$) inputs. *, $p<0.05$; **, $p<0.01$; ***, $p<0.001$.

**Figure 5 – Projection-specific differences in the overall, but not accumbal, inhibitory input to VP neurons.** (**A**) Schematic representation of the experimental setup. In each mouse, a retrograde tracer was injected into one of the four targets of the VP examined here and ChR2 was expressed in NAc neurons. Recordings were performed from identified VP projections and NAc input was induced optogenetically. (**B**) The proportion of responding VP neurons (i.e. the number of neurons displaying an oIPSC divided by the total number of neurons examined) was similar between projections and was between 66-77%. (**C-E**) The amplitude (**C**), paired-pulse ratio (**D**) and coefficient of variation (**E**) of the evoked oIPSC did not differ between projections (One-way ANOVA; $F_{(3,80)}=0.64$, $p=0.59$ for amplitude; $F_{(3,80)}=1.75$, $p=0.16$ for paired-pulse ratio; $F_{(3,80)}=1.08$, $p=0.36$ for CV of amplitude). (**F**) Application of 100 μM picrotoxin (GABA-A receptor blocker) on the slice completely blocked the oIPSCs in all VP projections, indicating these are GABA-only inputs. Inset – representative traces. (**G**) Cumulative probability of sPSC amplitudes in the four VP projections. There were no differences between the curves (Kolmogorov-Smirnov tests; $p>0.16$ for all pairwise comparisons between projections). (**H**) Cumulative probability of the frequency of sPSCs in the four VP projections. The $VP_{\rightarrow MDT}$ neurons showed significantly lower frequencies compared to the other projections (Kolmogorov-Smirnov tests; $d=0.13$, $p=0.0001$ compared to $VP_{\rightarrow LHb}$; $d=0.16$, $p<0.0001$ compared to $VP_{\rightarrow LH}$; $d=0.14$, $p<0.0001$ compared to $VP_{\rightarrow VTA}$). * - $p<0.05$ for MDT compared with each of the other projections. (**C-D**) Application of 100 μM picrotoxin (GABA-A receptor blocker) on the slice significantly reduced the frequency of spontaneous inputs in all projections (**I**), but the reduction was smaller for the $VP_{\rightarrow MDT}$ projections (reduction to 47.2±7 % of baseline) compared to all other projections (**J**) [One-way ANOVA main projection effect, $F_{(3,79)}=4.06$, $p=0.01$; post-hoc Tukey's multiple comparisons – compared to $VP_{\rightarrow LHB}$ (21.1±3 % of baseline), $p=0.001$, compared to $VP_{\rightarrow LH}$ (25.7±3 % of baseline), $p=0.02$, compared to $VP_{\rightarrow VTA}$ (26.9±5 % of baseline), $p=0.03$]. * - $p<0.05$ compared to $VP_{\rightarrow MDT}$ neurons.

**Figure 6 – $VP_{\rightarrow LH}$ neurons are more excitable and $VP_{\rightarrow VTA}$ neurons are less excitable than the average VP neuron**. (**A**) Experimental setup. VP projections were labeled by injecting a retrograde tracer in the target region and recorded from using whole-cell patch clamp electrophysiology. (**B**) Resting membrane potential was not different between the four VP projections we examined (One-way ANOVA, $F_{(3,103)}$=0.49, p=0.69; $VP_{\rightarrow MDT}$=-46.0±4.4 mV; $VP_{\rightarrow LHb}$=-45.8±4.0 mV; $VP_{\rightarrow LH}$=-46.6±5.8 mV; $VP_{\rightarrow VTA}$=-47.2±4.3 mV). (**C**) Action potential firing frequency at rest differed between the different VP projections (One-way ANOVA, $F_{(3,103)}$=3.47, p=0.02). Post-hoc analyses show that $VP_{\rightarrow LH}$ neurons fire in higher frequencies than $VP_{\rightarrow MDT}$ (Post-hoc Holm-Sidak's multiple comparisons test, p=0.03) and $VP_{\rightarrow VTA}$ (Post-hoc Holm-Sidak's multiple comparisons test, p=0.04) neurons. (**D**) Representative traces. (**E-F**) When applying a series of increasing depolarizing steps (inset, 20, 40, 60 and 80 pA) we found a main projection effect both in the number of action potentials per step (Analysis of covariance (ANCOVA), $F_{(3,260)}$=1.06, p=0.37 for slope comparison; $F_{(3,260)}$=6.1, p=0.0005 for elevation comparison) (**E**) and in the minimal latency to fire the first action potential (ANCOVA, $F_{(3,260)}$=4.65, p=0.003 for slope comparison) (**F**). Note that $VP_{\rightarrow LH}$ neurons had among the highest number of action potentials and shortest latency to fire, both of which indicate high excitability. (**G**) Representative traces. (**H**) An "Excitability index" was calculated by first calculating for each cell a z-score in each of the parameters recorded in panels B,C,E,F and then calculating the average z-score for each cell. There was a main projection effect for the z-scores (One-way ANOVA, $F_{(3,146)}$=3.21, p=0.03) and post-hoc analyses (Tukey's multiple comparisons test) revealed that the $VP_{\rightarrow LH}$ and the $VP_{\rightarrow VTA}$ projections were significantly different in their excitability (p=0.02). In addition, the excitability index of $VP_{\rightarrow LH}$ neurons was significantly higher than zero (One sample t-test, $t_{(36)}$=2.18, p=0.035) while that of $VP_{\rightarrow VTA}$ neurons was significantly lower than zero (One sample t-test, $t_{(31)}$=2.15, p=0.039). Thus, $VP_{\rightarrow LH}$ neurons are more excitable and $VP_{\rightarrow VTA}$ neurons are less excitable than the average VP neuron. * - p<0.05 compared to zero.

**Figure 7 - Distinct sets of genes related to ion transport are enriched within VTA-projecting and LH-projecting VP neurons. (A)** Upregulated genes within $VP_{\rightarrow LH}$ and $VP_{\rightarrow VTA}$ projection neurons were compared in a Venn diagram. Gene Ontology analysis identified common synaptic genes (**B**) in $VP_{\rightarrow VTA}$ and $VP_{\rightarrow LH}$ projection neurons (log fold changes from each projection type displayed in a heat map) and RFX3 as a predicted upstream regulator of a subset of genes related to ion transport. GO term analysis reveals distinct sets of ion transport-related genes and their listed potential upstream regulators within the $VP_{\rightarrow LH}$ (**C**) and $VP_{\rightarrow VTA}$ (**D**) projection neurons. ion transmem. transp. act. – ion transmembrane transporter activity, ext.-gly—gated ion ch. act – extracellular-glycine-gated ion channel activity, monov. Inorg. Cat. Transp. – monovalent inorganic cation transporter, reg. of synaptic trans. – regulation of synaptic transmission, cell. Metab. Processes – cellular metabolic processes.

**Figure 8 – Inhibiting $VP_{\rightarrow LH}$ neurons diminishes, while inhibiting $VP_{\rightarrow VTA}$ neurons enhances the preference for cocaine**. (**A**) Viral injection strategy. A retrograde AAV expressing Cre (rAAV-Cre) was injected into one of the 4 targets of the VP tested here and an AAV encoding Cre-dependently for the inhibitory DREADD hM4Di (AAV-DIO-hM4Di-eYFP) or a control sham virus (AAV-DIO-eYFP) were injected into the VP. (**B**) Cocaine CPP paradigm. After habituating to the CPP box, mice received daily alternating injections of cocaine (15 mg/kg i.p.) in one side of the box or saline in the other side of the box (4 injections of each). Mice then underwent 14 days of abstinence in their home-cages. On the test day, all mice first received an injection of CNO (3 mg/kg i.p.) 30 minutes prior to the beginning of the test and then were left in the CPP box for 15 minutes, during which their movement was recorded. A CPP score was calculated using the following equation - $CPP\ score = \frac{Time\ in\ cocaine-paired\ side - Time\ in\ saline-paired\ side}{Total\ time\ in\ the\ CPP\ box}$. (**C**) Inhibiting different VP projections had different influences on behavior (One-way ANOVA, $F_{(3,25)}$=5.81, p=0.004). While inhibiting $VP_{\rightarrow MDT}$ or $VP_{\rightarrow LHb}$ neurons did not affect the CPP score (One-sample t-test comparing to the CPP score of control mice expressing the sham virus and receiving CNO, Sham X CNO, 0.51; $t_{(6)}$=1.71, p=0.14 for $VP_{\rightarrow MDT}$, $t_{(5)}$=0.38, p=0.72 for $VP_{\rightarrow LHb}$), inhibiting the $VP_{\rightarrow LH}$ projection decreased the CPP score ($t_{(7)}$=2.54, p=0.039) and inhibiting the $VP_{\rightarrow VTA}$ projection increased the CPP score ($t_{(7)}$=3.42, p=0.011). (**D-H**) Heatmaps of the movement of representative mice from all groups. (**I**) Inhibiting the different VP projections did not affect the distance traveled differently between projections.

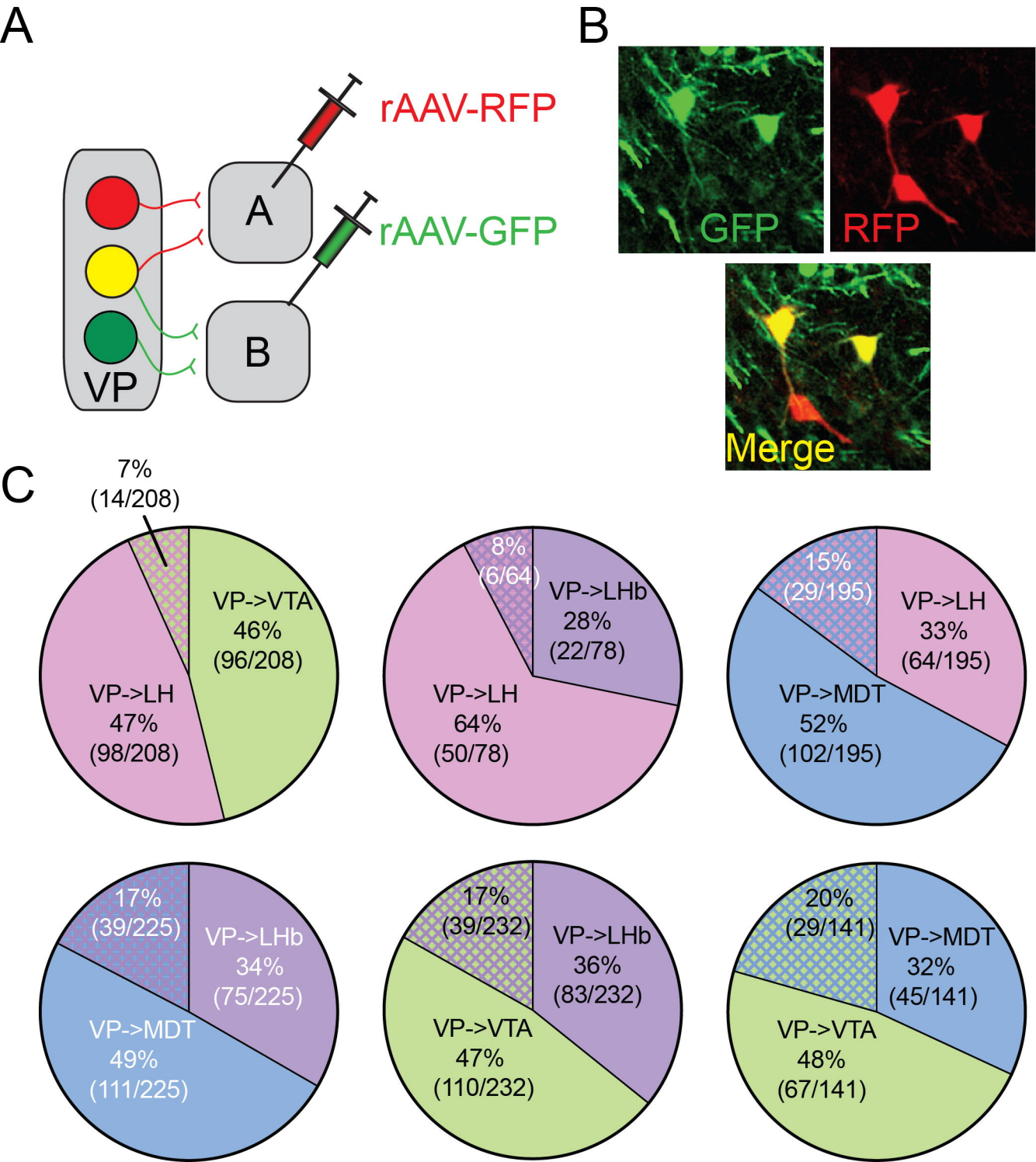
A
rAAV-RFP
rAAV-GFP
A
B
VP
B
GFP
RFP
Merge
C
7%
(14/208)
VP->VTA
46%
(96/208)
VP->LH
47%
(98/208)
8%
(6/64)
VP->LHb
28%
(22/78)
VP->LH
64%
(50/78)
15%
(29/195)
VP->LH
33%
(64/195)
VP->MDT
52%
(102/195)
17%
(39/225)
VP->LHb
34%
(75/225)
VP->MDT
49%
(111/225)
17%
(39/232)
VP->LHb
36%
(83/232)
VP->VTA
47%
(110/232)
20%
(29/141)
VP->MDT
32%
(45/141)
VP->VTA
48%
(67/141)

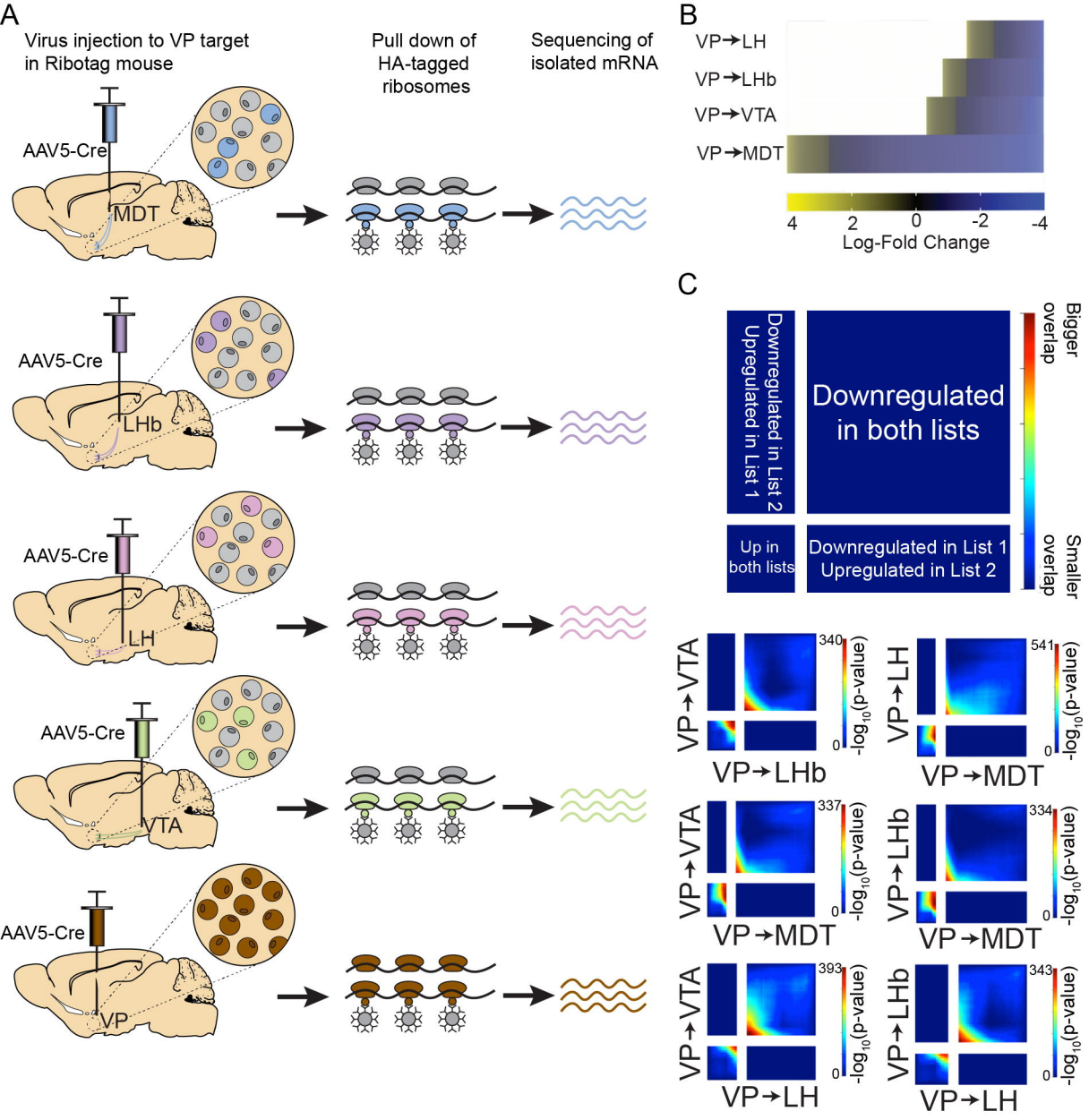
A
Virus injection to VP target in Ribotag mouse
Pull down of HA-tagged ribosomes
Sequencing of isolated mRNA
AAV5-Cre
MDT
LHb
LH
VTA
VP
B
VP→LH
VP→LHb
VP→VTA
VP→MDT
4
2
0
-2
-4
Log-Fold Change
C
Downregulated in List 2 Upregulated in List 1
Downregulated in both lists
Up in both lists
Downregulated in List 1 Upregulated in List 2
Bigger overlap
Smaller overlap
VP→VTA
VP→LHb
340
VP→LH
VP→MDT
541
VP→VTA
VP→MDT
337
VP→LHb
VP→MDT
334
VP→VTA
VP→LH
393
VP→LHb
VP→LH
343
-log10(p-value)
0

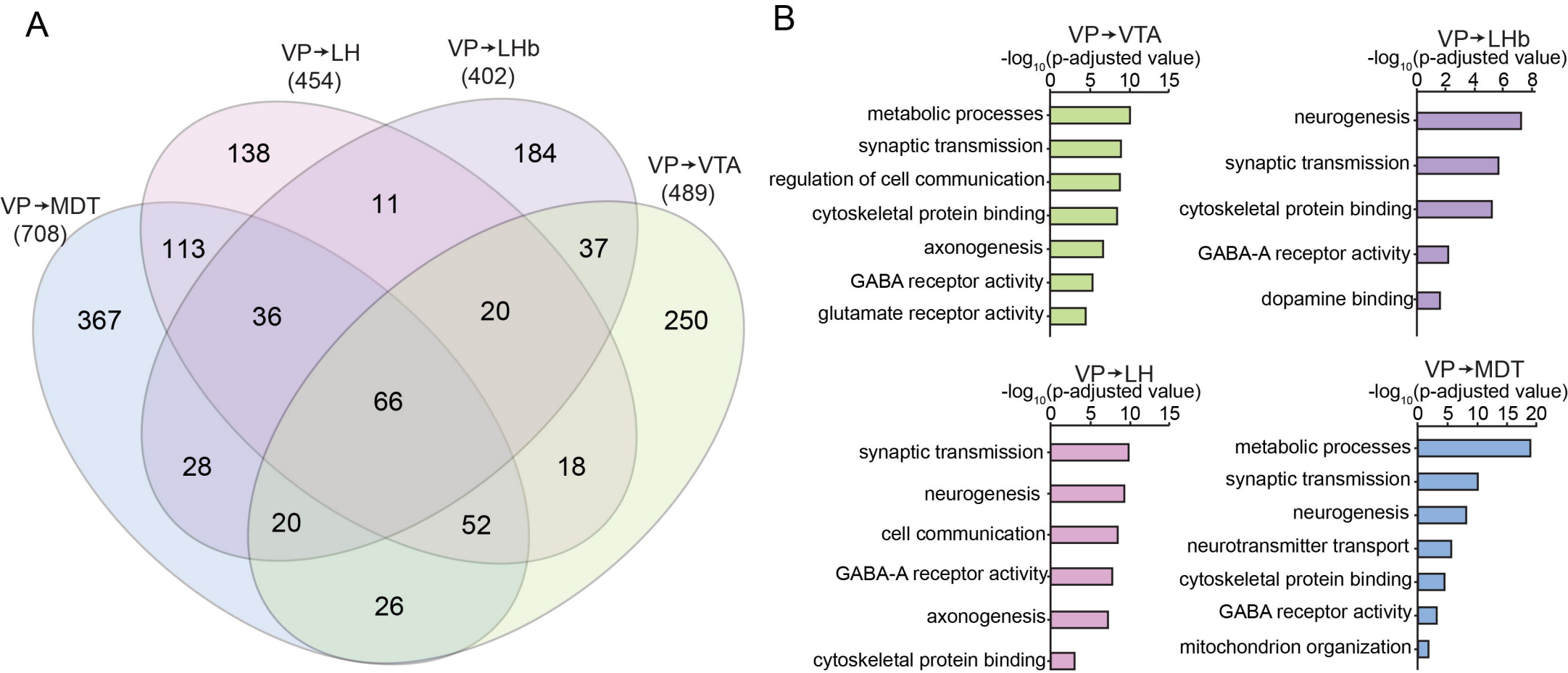
A
VP→LH
(454)
VP→LHb
(402)
VP→VTA
(489)
VP→MDT
(708)
138
184
11
113
37
367
36
20
250
66
28
18
20
52
26
B
VP→VTA
-log10(p-adjusted value)
0 5 10 15
metabolic processes
synaptic transmission
regulation of cell communication
cytoskeletal protein binding
axonogenesis
GABA receptor activity
glutamate receptor activity
VP→LHb
-log10(p-adjusted value)
0 2 4 6 8
neurogenesis
synaptic transmission
cytoskeletal protein binding
GABA-A receptor activity
dopamine binding
VP→LH
-log10(p-adjusted value)
0 5 10 15
synaptic transmission
neurogenesis
cell communication
GABA-A receptor activity
axonogenesis
cytoskeletal protein binding
VP→MDT
-log10(p-adjusted value)
0 5 10 15 20
metabolic processes
synaptic transmission
neurogenesis
neurotransmitter transport
cytoskeletal protein binding
GABA receptor activity
mitochondrion organization

A

Day 1 → Day 14 → Day 21 → Clearing → Imaging

rAAV-Cre | RVdG | Euth. | iDisco+ | LSFM

AAV-FLEx-G

AAV-FLEx-TVA

Analysis

ClearMap

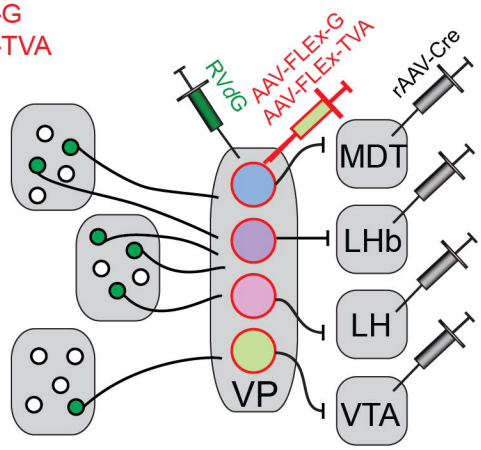


B

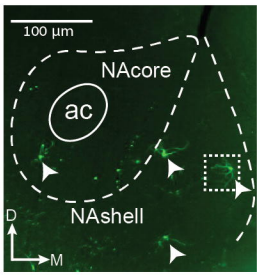


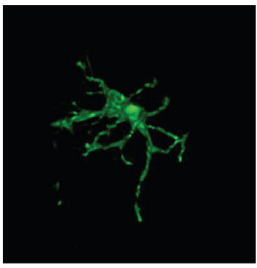

C

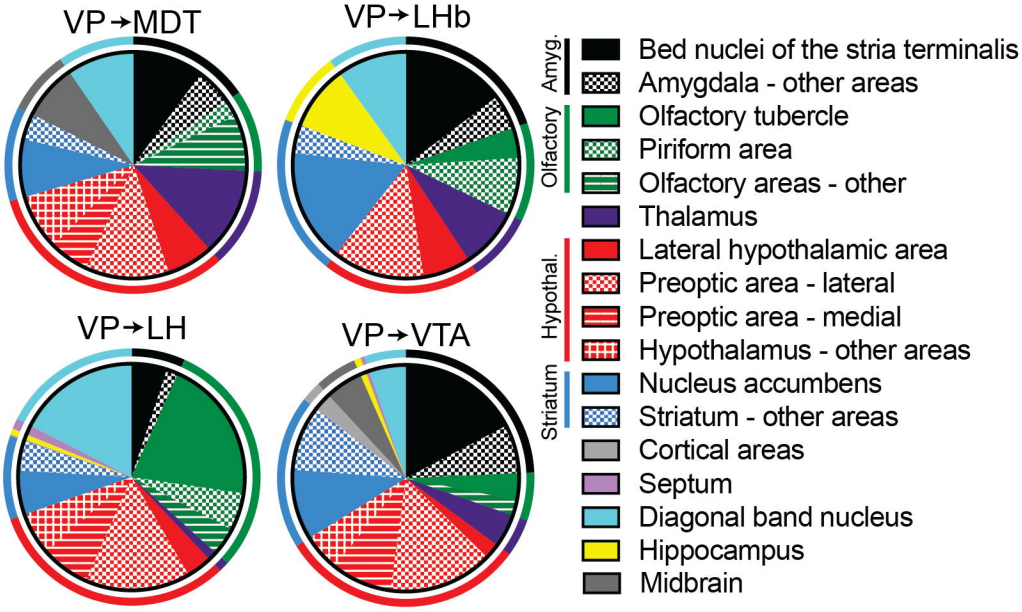


D

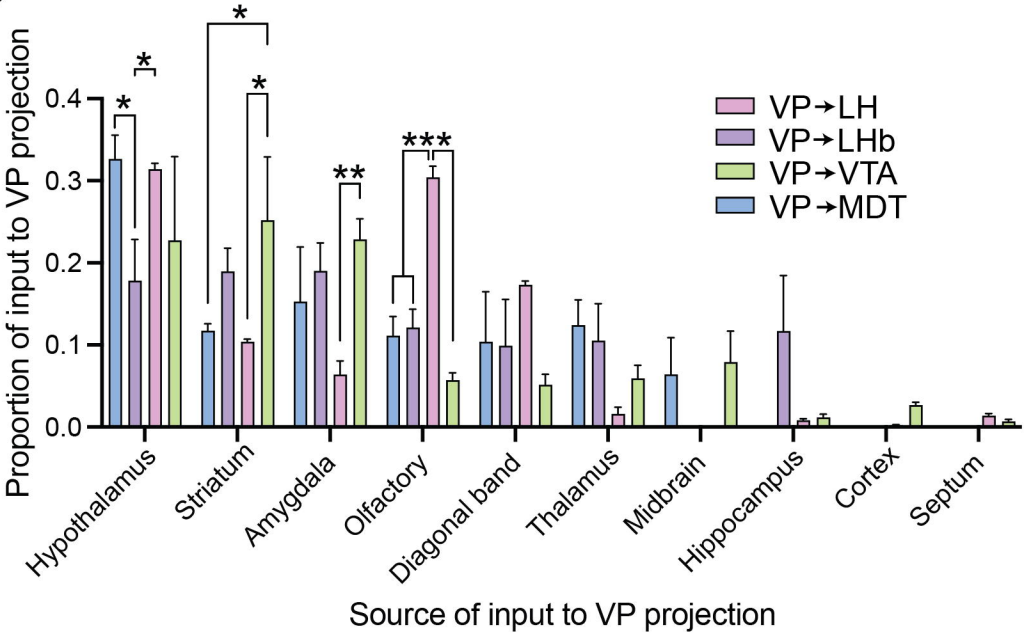

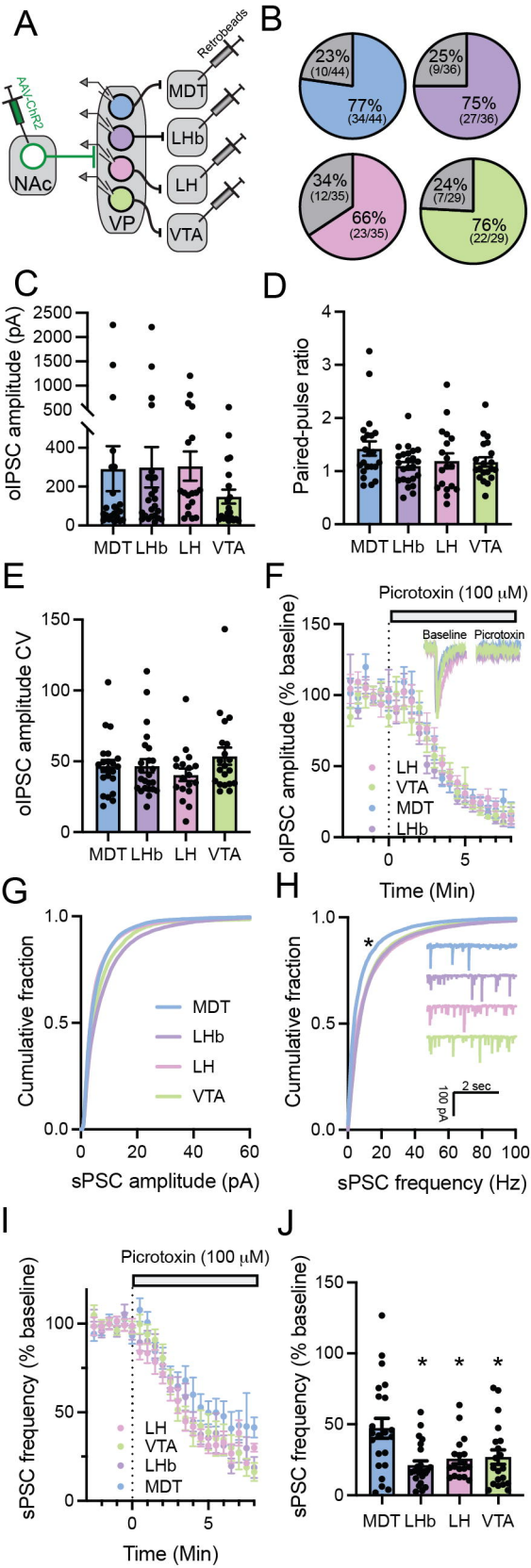
A
Retrobeads
AAV-ChR2
NAc
VP
MDT
LHb
LH
VTA
B
23% (10/44)
77% (34/44)
25% (9/36)
75% (27/36)
34% (12/35)
66% (23/35)
24% (7/29)
76% (22/29)
C
oIPSC amplitude (pA)
MDT LHb LH VTA
D
Paired-pulse ratio
MDT LHb LH VTA
E
oIPSC amplitude CV
MDT LHb LH VTA
F
Picrotoxin (100 μM)
Baseline
Picrotoxin
oIPSC amplitude (% baseline)
LH
VTA
MDT
LHb
Time (Min)
G
Cumulative fraction
MDT
LHb
LH
VTA
sPSC amplitude (pA)
H
Cumulative fraction
*
2 sec
100 pA
sPSC frequency (Hz)
I
Picrotoxin (100 μM)
sPSC frequency (% baseline)
LH
VTA
LHb
MDT
Time (Min)
J
sPSC frequency (% baseline)
MDT LHb LH VTA

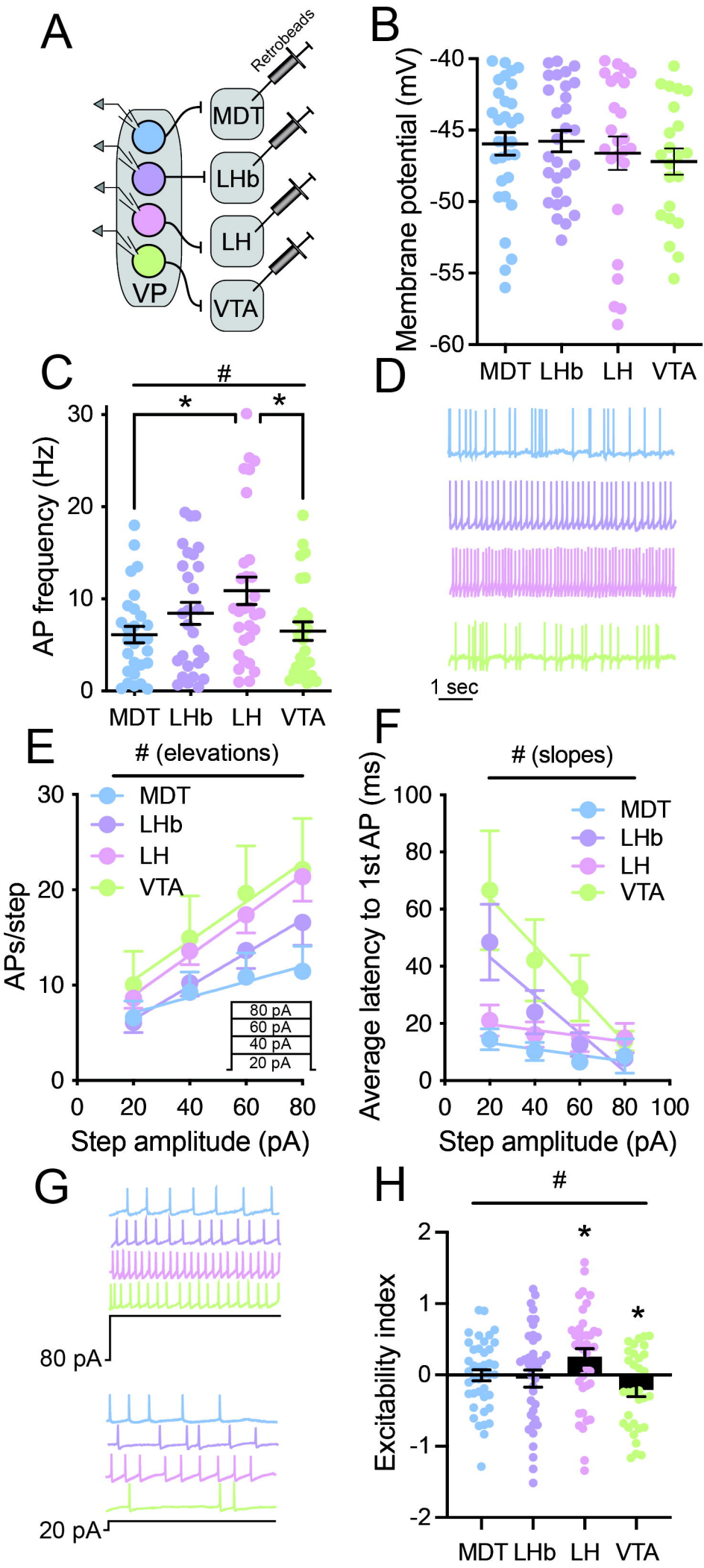
A
Retrobeads
MDT
LHb
LH
VTA
VP
B
Membrane potential (mV)
-40
-45
-50
-55
-60
MDT LHb LH VTA
C
#
*
*
AP frequency (Hz)
30
20
10
0
MDT LHb LH VTA
D
1 sec
E
# (elevations)
MDT
LHb
LH
VTA
APs/step
30
20
10
0
80 pA
60 pA
40 pA
20 pA
0 20 40 60 80
Step amplitude (pA)
F
# (slopes)
MDT
LHb
LH
VTA
Average latency to 1st AP (ms)
100
80
60
40
20
0
0 20 40 60 80 100
Step amplitude (pA)
G
80 pA
20 pA
H
#
*
*
Excitability index
2
1
0
-1
-2
MDT LHb LH VTA

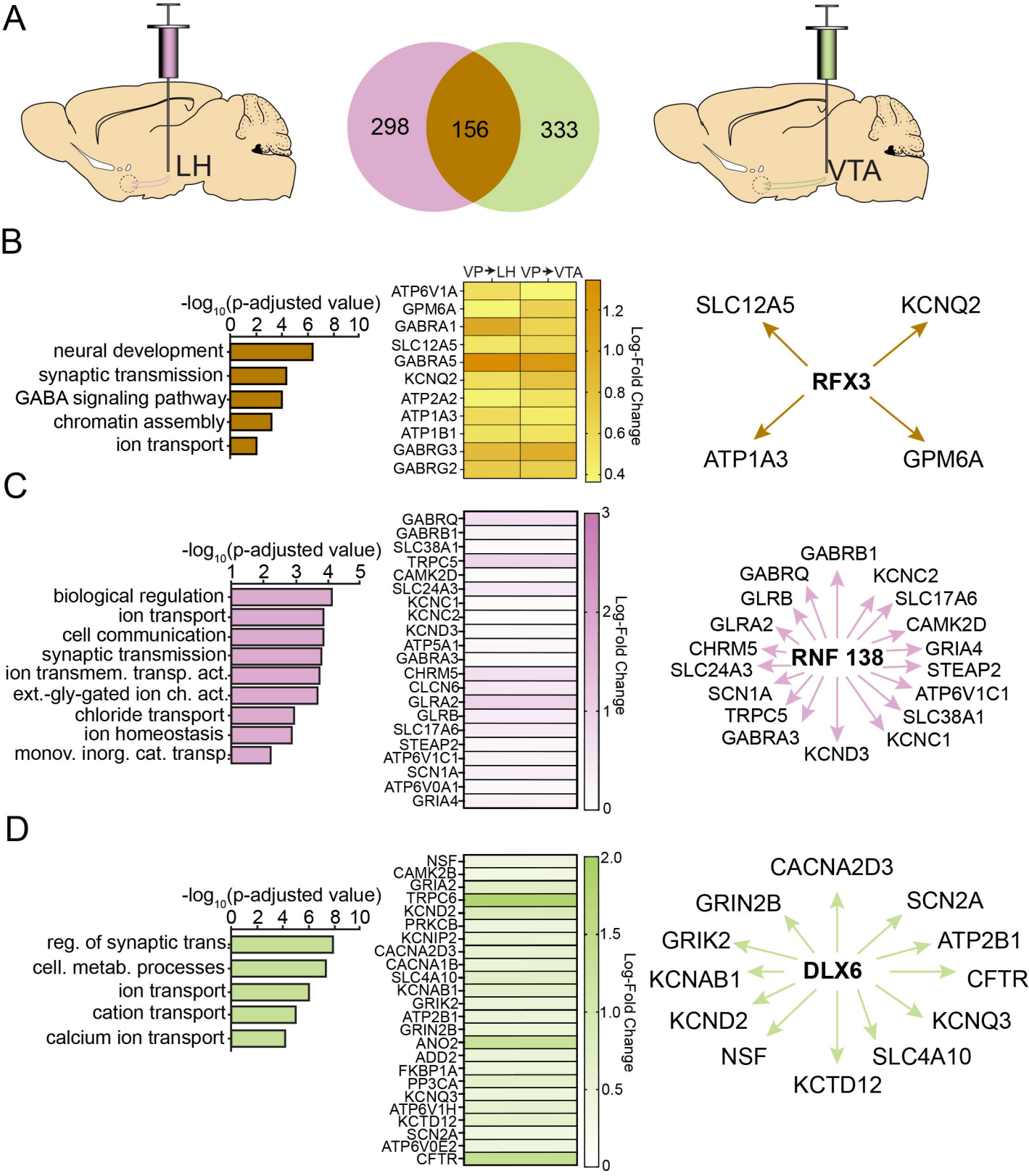
A
LH
298
156
333
VTA
B
-log10(p-adjusted value)
0 2 4 6 8 10
neural development
synaptic transmission
GABA signaling pathway
chromatin assembly
ion transport
VP→LH VP→VTA
ATP6V1A
GPM6A
GABRA1
SLC12A5
GABRA5
KCNQ2
ATP2A2
ATP1A3
ATP1B1
GABRG3
GABRG2
Log-Fold Change
1.2
1.0
0.8
0.6
0.4
SLC12A5
KCNQ2
RFX3
ATP1A3
GPM6A
C
-log10(p-adjusted value)
1 2 3 4 5
biological regulation
ion transport
cell communication
synaptic transmission
ion transmem. transp. act.
ext.-gly-gated ion ch. act.
chloride transport
ion homeostasis
monov. inorg. cat. transp.
GABRQ
GABRB1
SLC38A1
TRPC5
CAMK2D
SLC24A3
KCNC1
KCNC2
KCND3
ATP5A1
GABRA3
CHRM5
CLCN6
GLRA2
GLRB
SLC17A6
STEAP2
ATP6V1C1
SCN1A
ATP6V0A1
GRIA4
Log-Fold Change
3
2
1
0
GABRB1
GABRQ
KCNC2
GLRB
SLC17A6
GLRA2
CAMK2D
CHRM5
GRIA4
SLC24A3
RNF 138
STEAP2
SCN1A
ATP6V1C1
TRPC5
SLC38A1
GABRA3
KCNC1
KCND3
D
-log10(p-adjusted value)
0 2 4 6 8 10
reg. of synaptic trans.
cell. metab. processes
ion transport
cation transport
calcium ion transport
NSF
CAMK2B
GRIA2
TRPC6
KCND2
PRKCB
KCNIP2
CACNA2D3
CACNA1B
SLC4A10
KCNAB1
GRIK2
ATP2B1
GRIN2B
ANO2
ADD2
FKBP1A
PP3CA
KCNQ3
ATP6V1H
KCTD12
SCN2A
ATP6V0E2
CFTR
Log-Fold Change
2.0
1.5
1.0
0.5
0
CACNA2D3
GRIN2B
SCN2A
GRIK2
ATP2B1
KCNAB1
DLX6
CFTR
KCND2
KCNQ3
NSF
SLC4A10
KCTD12

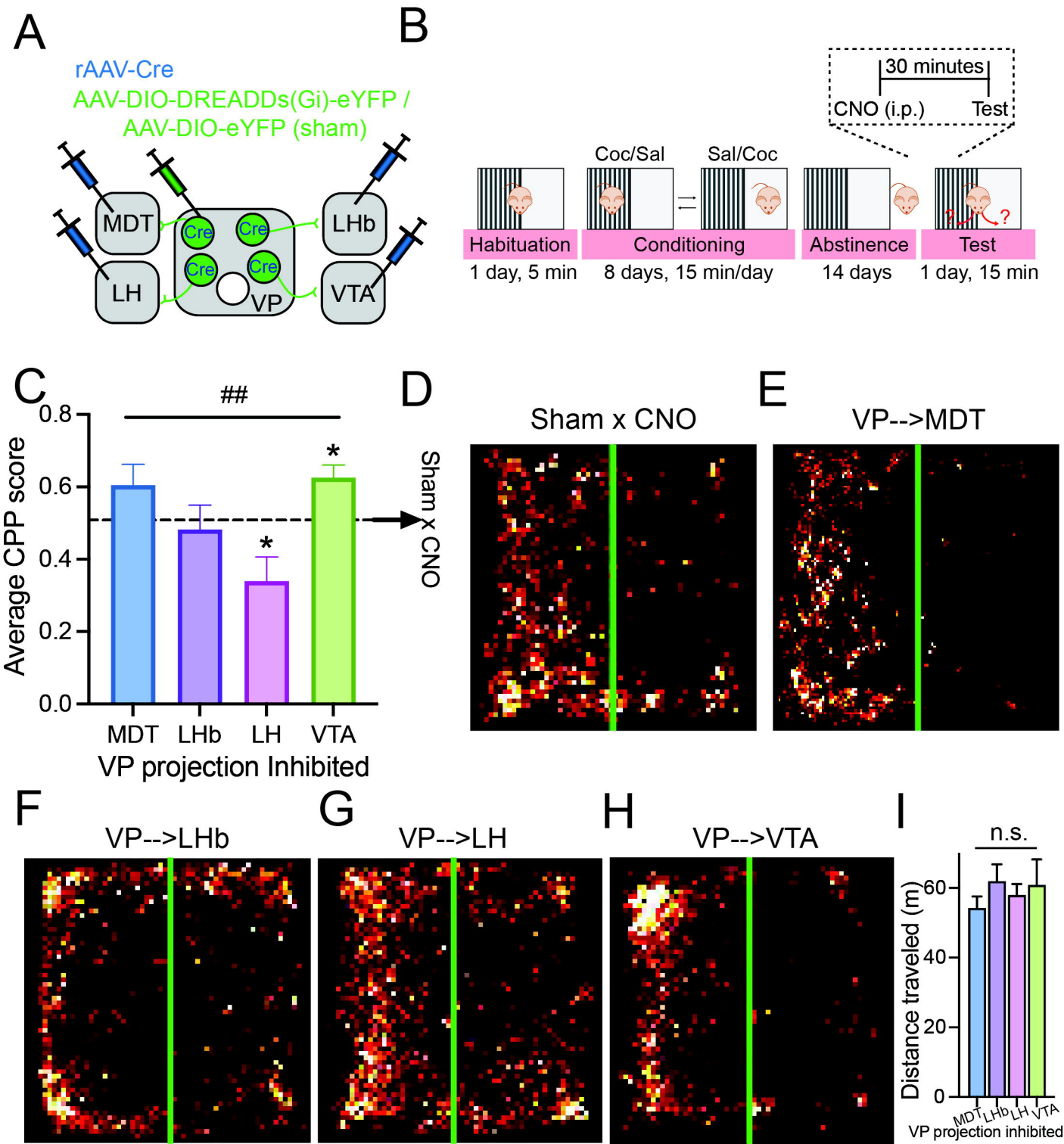
A
rAAV-Cre
AAV-DIO-DREADDs(Gi)-eYFP /
AAV-DIO-eYFP (sham)
MDT
LH
LHb
VTA
VP
Cre
B
30 minutes
CNO (i.p.)
Test
Coc/Sal
Sal/Coc
Habituation
Conditioning
Abstinence
Test
1 day, 5 min
8 days, 15 min/day
14 days
1 day, 15 min
C
##
Average CPP score
0.8
0.6
0.4
0.2
0.0
*
*
Sham x CNO
MDT
LHb
LH
VTA
VP projection Inhibited
D
Sham x CNO
E
VP-->MDT
F
VP-->LHb
G
VP-->LH
H
VP-->VTA
I
n.s.
Distance traveled (m)
60
40
20
0
MDT
LHb
LH
VTA
VP projection inhibited